



## 저작자표시-비영리-변경금지 2.0 대한민국

이용자는 아래의 조건을 따르는 경우에 한하여 자유롭게

- 이 저작물을 복제, 배포, 전송, 전시, 공연 및 방송할 수 있습니다.

다음과 같은 조건을 따라야 합니다:



저작자표시. 귀하는 원저작자를 표시하여야 합니다.



비영리. 귀하는 이 저작물을 영리 목적으로 이용할 수 없습니다.



변경금지. 귀하는 이 저작물을 개작, 변형 또는 가공할 수 없습니다.

- 귀하는, 이 저작물의 재이용이나 배포의 경우, 이 저작물에 적용된 이용허락조건을 명확하게 나타내어야 합니다.
- 저작권자로부터 별도의 허가를 받으면 이러한 조건들은 적용되지 않습니다.

저작권법에 따른 이용자의 권리는 위의 내용에 의하여 영향을 받지 않습니다.

이것은 [이용허락규약\(Legal Code\)](#)을 이해하기 쉽게 요약한 것입니다.

[Disclaimer](#)

공학박사 학위논문

# **Stretchable Skin-like Thermo-haptic Device for Artificial Thermal Sensation in Virtual Reality**

가상현실에서 인공 열감 재현을 위한 열-햅틱 전자 피부에 관한 연구

2021 년 2 월

서울대학교 대학원

기계공학부

이진우

# Stretchable Skin-like Thermo-haptic Device for Artificial Thermal Sensation in Virtual Reality

가상현실에서 인공 열감 재현을 위한 열-햅틱 전자 피부에 관한 연구

지도교수 고 승 환

이 논문을 공학박사 학위논문으로 제출함

2020 년 10 월

서울대학교 대학원

기계공학부

이 진 우

이진우의 공학박사 학위논문을 인준함

2020 년 12 월

위 원 장 : 이동준

(인)

부위원장 : 고승환

(인)

위 원 : 도형록

(인)

위 원 : 권진형

(인)

위 원 : 홍석준

(인)

## **Abstract**

Along with the tactile sensation, thermal sensation by temperature feeling on skin can provide rich physical information on the environment. Temperature is an effective means of communication in our life since human skin detects a broad range of temperature in high resolution. With a simple touch of an object, human can sense the relative temperature and even distinguish objects of different thermal conductivities without any visual cue. Thus, artificially reproducing accurate and controllable thermal sensation haptic signal on human epidermis will certainly be a major research area to reconstruct the more realistic virtual reality (VR) environment.

In this study, for the first time (to the best of authors' knowledge), a skin-like, highly soft and stretchable and bi-functional (both cold and hot sensation) thermo-haptic device is reported for wearable VR applications, capable of simple switching cold and warm sensations by changing heat flux direction with a single device structure (not separate heater and cooler). The skin-like thermo-haptic device can actively cool down and heat up the deformable skin surface with an instantaneous and accurate adjustment of temperature based upon a feedback control algorithm to mimic desirable thermal sensation with maximum stretching over 230% using a thermally engineered stretchable backbone and serpentine interconnecting electrode. As a proof-of-concept, the skin-like thermo-haptic device was integrated with the finger-motion tracking glove to provide an artificial thermal sensation information to skin in various situation such as touching a cold beer bottle and a hot coffee cup in a virtual space. This new types of skin-like thermo-haptic device can offer potential implications for a next-generation haptic device to provide a unique thermal information for the more realistic virtual world field.

**keywords : Skin-like electronics, artificial thermal sensation, stretchable cooler/heater, virtual reality**

**Student number: 2016-30180**

# Table of content

<b>Chapter 1: Introduction</b>	<b>1</b>
1.1. Background	1
1.2. Previous studies	2
1.3. Objective and preview of this study	5
<b>Chapter 2: Methods</b>	<b>5</b>
2.1. Material preparation	5
2.2. Electrode fabrication	6
2.3. Characterization and performance examination	7
2.4. A hand-shaped PDMS cooling/heating and thermo-haptic VR application	7
<b>Chapter 3: Designing the stretchable thermo-haptic device</b>	<b>8</b>
3.1. Schematic illustrations and basic operating mechanisms	8
3.2. Optimizing the design parameters of the serpentine Cu electrode	10
3.3. Optimizing the design parameters of thermoelectric semiconductor pellets	14
3.4. Selective thermal engineering of the device architecture	17
<b>Chapter 4: Characterization and performance evaluation of the device</b>	<b>24</b>
4.1. Cooling and heating performance of stretchable thermo-haptic device	24
4.2. Reversed mode for accurate and desirable thermal sensation	27

4.3.	Mechanical robustness of the device against various stress-----	30
<b>Chapter 5: Wearable personal thermal management-----</b>		<b>32</b>
5.	Examining the device potential to for wearable personal thermal management-- -----	32
<b>Chapter 6: Reconstruction of artificial thermal feeling with the stretchable thermo-haptic device in VR space-----</b>		<b>34</b>
6.1.	Integration of device to the finger motion tracking glove-----	34
6.2.	Replicating the thermal sensation of virtual objects at various temperature---	35
6.3.	Replicating the thermal sensation of virtual objects with different thermal conductivities-----	37
<b>Chapter 7: Conclusion-----</b>		<b>39</b>
<b>Reference-----</b>		<b>40</b>
<b>Abstract-----</b>		<b>42</b>

# Chapter 1

## Introduction

### 1.1. Background

Virtual and augmented reality (VR and AR, respectively) reproduce a realistic and highly immersive experience by artificially reconstructing various human senses and delivering perceptual information to the sensory system. This technology allows events or environments that cannot be encountered in real life to be experienced, such as visiting an otherwise inaccessible place or meeting a person that does not exist in reality. In addition to their use in the gaming and entertainment industries, VR and AR have also had an impact on a variety of areas such as virtual commerce, real estate, health care, and education. [1]

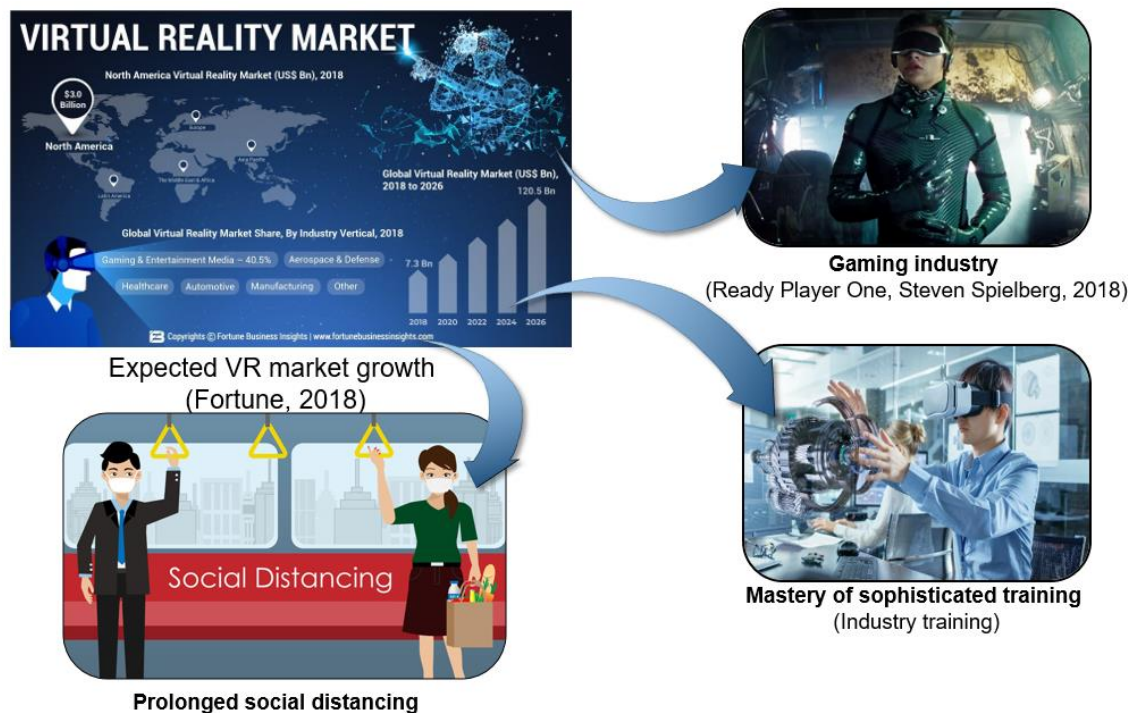


**Figure 1.1:** The schematic that shows the anticipated growth of the VR and AR and their practical applications. [2] [3] [4] [5]



Significant effort has been dedicated to artificially imitating the human senses in VR and AR applications, but most commercial devices concentrate on visual and auditory cues. In comparison, there has been little advance in the replication of tactile senses [6] [7] [8] [9] [10] [11], which include temperature, vibration, texture, pressure and pain. Of the tactile senses associated with the human skin, thermal sensation plays the most significant role due to the constant exchange of heat with other thermal entities via physical contact. In addition to simple temperature sensing, the human body can differentiate by touch objects with different thermal conductivities even at the same temperature. Different types of thermoreceptor, or temperature-sensing arrays, in the skin are able to sense independent temperature zones, allowing a wide temperature window of 4 °C to 52 °C to be perceived at a precise detection resolution of 0.02 K.<sup>[12]</sup> Due to the high sensitivity of thermoreceptors, the body can transform neural signals into a refined sense of thermal perception, which means artificially replicating thermo-haptic signals is possible but difficult.



**Figure 1.2:** 5 types of tactile senses which are temperature, vibration, texture, pressure and pain

## 1.2. Previous studies

In this regard, various studies have been dedicated to artificially restructure the human senses, and much of these efforts served to be valuable assets in VR applications, but most of the reported virtual haptic devices consist of the rigid and bulky structure<sup>[13] [14] [15] [16] [17] [18] [19]</sup>, lowering skin-compatibility and ultimately decreasing heat conduction from or to human epidermis due to the smaller thermal contact area. For this reason, most of the soft thermo-haptic device has been realized only in heating function<sup>[20] [21] [22]</sup>, never in a soft cooling function in a skin-like form. Only heating can make limited half function of the artificial thermal feeling in a thermal sensation device. To realize the true artificial thermal sensation for thermo-haptic device, both heating and cooling sensation functionality needs to be realized in a soft skin-like device form. Furthermore, the cooling and heating functionality needs to be demonstrated by a single device, not by separate heaters and coolers.



**Figure 1.3:** Previously commercialized thermo-haptic devices for VR/AR applications.<sup>[19]</sup>

Along with the soft and stretchable property, a thermo-haptic device must be capable of actively heating and cooling with a high degree of controllability in a range from 15°C to 45°C (below or above which would result in pain or tissue damages<sup>[23]</sup>) in order to reproduce desirable thermal sensation on human epidermis. Cooling the human skin is of critical importance especially in the thermo-haptic device, since human epidermal temperature is generally higher than room-temperature, implicating that a wide portion of temperature spectrum cannot be realized, if the device can only heat human skin. Another potential advantage of the device with an interchangeable cooling and heating ability lies upon its capacity to reach target temperature and rapidly return to original temperature. For example, if it were to emulate a thermal situation of touching a beer bottle at 15°C for a moment, the device must heat up to the room-temperature instantly after it cools down to 15°C to remove unintended residual thermal sensation.



**Figure 1.4:** the photographic figure of the wearable thermo-haptic device that is capable of reconstructing the cold and warm sensation in the virtual environment

### **1.3. Objective and preview of this study**

Therefore, in this study, a highly stretchable and skin-like thermo-haptic device to provide an artificial hot and cold thermal sensation to skin was demonstrated for wearable cutaneous VR applications based upon a thermally conductive elastomer backbone and thermoelectric materials, connected with stretchable interconnecting electrode, which enables heat transfer under maximum stretching over 230%. The skin-like thermo-haptic device can work in a bi-functional mode (heating and cooling mode) in a single device, not by assembling separate heating device and cooling device like most wearable thermal management devices either as a cooler only or heater only [20] [24] [25] [26] [27]. As aforementioned, another unique highlight of stretchable thermo-haptic device is its ability to reach target temperature and rapidly return to original temperature within a few seconds by changing the direction of current (thus heat flux direction), instead of relying on rather far less effective natural convection. This enables generation of desirable fast thermal sensation without subsequent unintended parasitic thermal residue after switching device operation mode, allowing the stretchable thermo-haptic device to realize various virtual situations with higher accuracy. Finally, to fully verify the practical feasibility of the stretchable thermo-haptic device in wearable VR applications, a variety of real-life thermally interacting situations such as holding a chilly beer bottle and a hot coffee mug were virtually reproduced with the devices mounted on the previously developed finger-motion tractable glove<sup>[28]</sup>.

## **Chapter 2**

### **Methods**

## 2.1. Material preparation

A thermally conductive metal-elastomer composite (AFE) was prepared by shear-mixing Ag flake (Sigma Aldrich) and Ecoflex (EcoFlex00-30, Smooth-on) at 60% wt. ratio respectively until uniform homogeneity is attained. Then, the mixture was spin-cast on a plastic Petri dish by using the laboratory spin coater at 400 rpm for 60 seconds and cured at 60 °C for 10 minutes to produce a thin layer (~150  $\mu\text{m}$ ) of a metal-elastomer mixture.

## 2.2. Electrode fabrication

Polyimide solution (Dongbaek Fine-Chem) was first spin-coated on one side of 25  $\mu\text{m}$  thick Cu foil (Alfa Aesar) at 2000 rpm. The Cu foil is then heated at 140 °C for 4 min on a laboratory hot-plate and at 250°C for 1hr at  $\text{N}_2$  atmosphere to prevent oxidation of the Cu foil. Next, a polyimide-coated Cu foil is placed upon AFE with a polyimide-free Cu side facing up and laser-ablated (Nanio Air 355–3-V, Innolas,  $\lambda=355\text{nm}$ ) with a serpentine pattern based upon COMSOL numerical simulation, followed by peeling off the rest of PI coated Cu foil. AFE was then spin-coated on the Cu electrode at 400 rpm and cured at 60°C for 10 minutes to encapsulate the serpentine electrode and further to enhance mechanical stability. Two thin encapsulating layers of AFE serve to mechanically retain the shape of the serpentine as it stretches and return to its original shape. Since AFE is electrically insulating, circular holes ( $r=1.25\text{mm}$ ) are laser-patterned and carefully peeled off to expose Cu for electrical connection as in **Figure 2.1**.

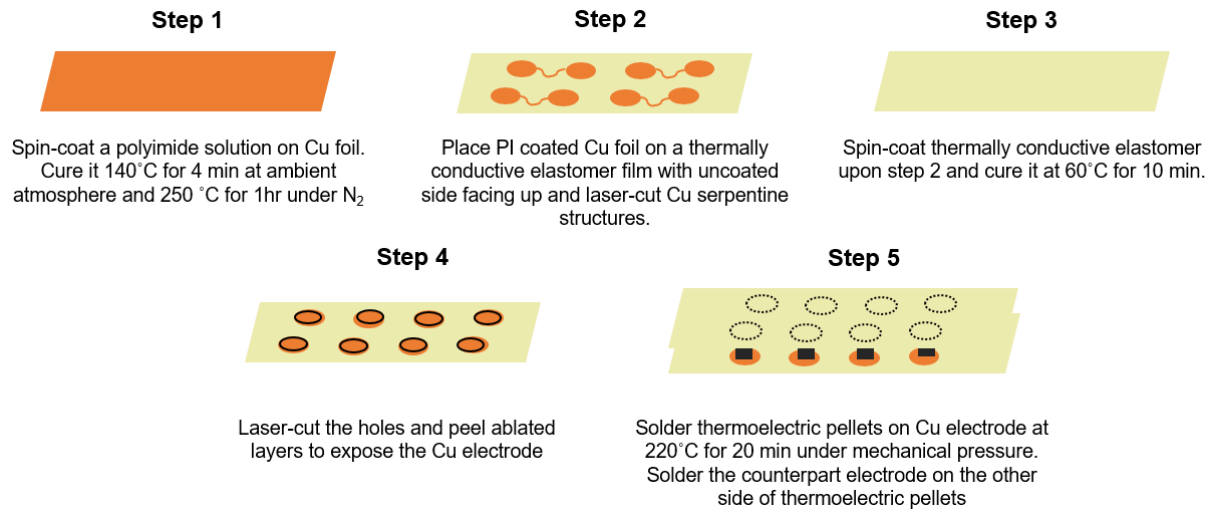


**Figure 2.1** Schematic representation of the device fabrication process. Note that thermoelectric pellets in the fabrication process as shown above are connected in series within the device and thus operate as a whole.

A counterpart serpentine electrode was fabricated using the same process. Then, p, n type 1.6mm·1.6mm·1.7mm thermoelectric pellets (Wuhan Xinrong New Materials) were soldered on the Cu exposed circular holes at 220 °C for 20 minutes under mechanical pressure in N<sub>2</sub> atmosphere (spacing between thermoelectric pellets is 3.5mm.). The final device is fabricated when the counterpart electrode was soldered on the other side of thermoelectric pellets utilizing the same process as it can be seen in **Figure 2.2**

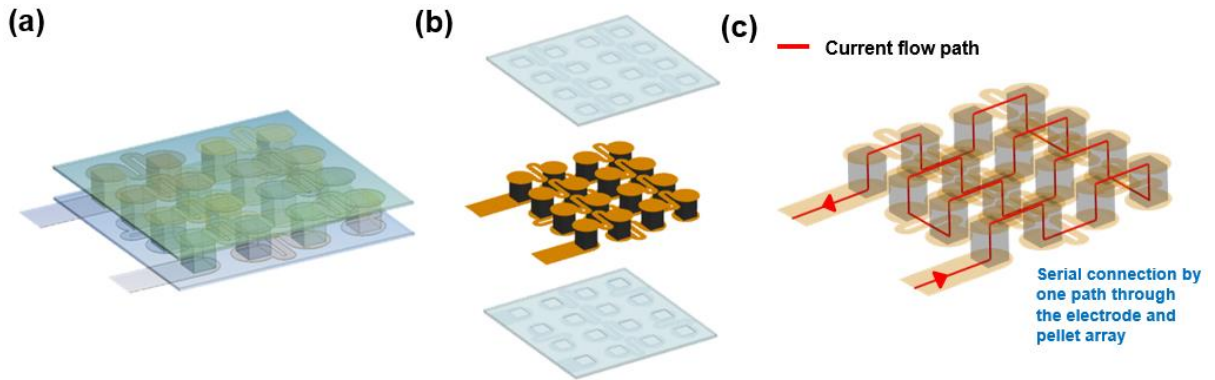


**Figure 2.2:** 3D Visual representation of the complete device structure comprising AFE, Cu serpentine electrode and thermoelectric pellet, which are all connected in series.

### 2.3. Characterization and performance examination

Heat flux during cooling and heating mode data was acquired at various DC constant current points using a commercial heat flux sensor (FluxTeq) with a device sandwiched between an insulator and a heat flux sensor under mechanical pressure. Thermal conductivity of Ag flake/Ecoflex of a different ratio (0 wt%, 20 wt%, 40 wt% and 60 wt%) was measured using a laser flash Apparatus (Netzsch LFA 467) and differential scanning calorimeter (DSC204 F1 Phoenix). All the temperature profile measurements and visual images were collected with infrared (IR) camera (FLIR A645 sc), and cyclic heating/cooling test was conducted using two DC power supplies programmed with Arduino kit. The laboratory-made automated cyclic motion controller was used to examine a stretching test while obtaining the temperature profile with IR camera or electrical resistance change with a source meter (Keithley, Model-2400).

#### **2.4. A hand-shaped PDMS cooling/heating and thermo-haptic VR application**

A hand-shaped mold was illustrated with AutoCAD and fabricated by a 3D printer (Sindoh dp200). Two parts of PDMS (Dow Corning Sylgard 184) were mixed in a ratio of 10:1 and degassed under vacuum for 30 minutes. Then, degassed PDMS is poured into the mold and cured at room-temperature on the optics table. To mimic the conditions of a human hand epidermis, a hand-shaped PDMS was heated at 35 °C for 5 minutes and placed upon 27mm x 27mm device. The device cooled and heated the PDMS at 1.5 A and 0.65 A respectively using DC power supplies.

## **Chapter 3**

### **Designing the stretchable thermo-haptic device**

#### **3.1. Schematic illustrations and basic operating mechanisms**

Schematic illustrations of thermo-haptic device, which consists of a visual

representation of the final product framework and an exploded view of the multiple interfacial materials, comprise **Figure 3.1a** The laser-ablated serpentine Cu electrode, which is coated with polyimide on one side and encapsulated with a thin film of thermally conductive elastomer, serves to electrically interconnect alternating p-type and n-type thermoelectric pellets that are responsible for inducing a rapid thermal response when voltage is applied. Due to its highly deformable structure, the Cu serpentine electrode, embedded in a thermally conductive elastomer, withstands a high degree of bi-directional strain while sustaining the electrical circuit with extremely low electrical resistance. Incorporating Ag flake into Ecoflex produces a thermally conductive stretchable substrate, which heightens the device performance and functions as a mechanical backbone in the device architecture. The finalized design of the device as in **Figure 3.1b** can cool down and heat up the body surface by simply switching the direction of electrical current.

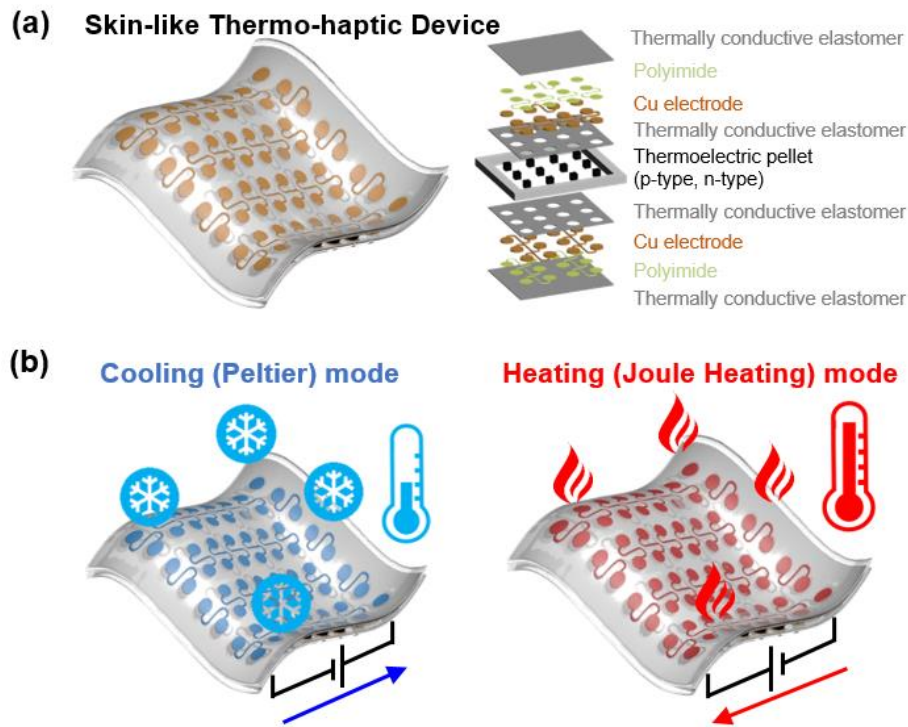


**Figure 3.1:** Simplified representation of the thermo-haptic device (a) Simplified illustration of the finalized Peltier device and the exploded view of interfacial materials and laser-ablated serpentine electrode that constitute the device. (b) Schematic that shows the device can be used to cool down or heat up the user's body temperature according to the electrical current direction.



### 3.2. Optimizing the design parameters of the serpentine Cu electrode

Numerical simulation and experimental validation corroborate the Cu serpentine interconnection electrode design, making the device less vulnerable to stretching and deformation while maintaining its electrical conductivity. Since non-uniform distribution of charged carriers induces a temperature discrepancy in thermoelectric materials, the device requires extremely low resistance to generate temperature difference. Yet, making the metal electrode highly stretchable involves a large reduction in the thickness and width of the electrode in a form of the serpentine structure, which directly results in resistance degradation as a trade-off. In **Figure 3.2**, it was predicted that there must exist an optimal point that balances mechanical and electrical properties with a minimum trade-off. In order to locate this point, the electrode design parameters were numerically calculated using COMSOL, and determined the Cu serpentine electrode specification by experimentally comparing cooling capacity under the cooling mode. The electrode was experimentally validated only for the cooling mode, because thermoelectric cooling is intrinsically counteracted by Joule heating as in Supplementary Information Note 1, making cooling much more challenging than heating.

$$Q_c = 2N(\alpha IT_c - k\Delta T - \frac{1}{2}R_e I^2) \text{ for the cooling mode}$$

$$Q_h = 2N(\alpha IT_h - k\Delta T + \frac{1}{2}R_e I^2) \text{ for the heating mode}$$

where the first term in the parenthesis signifies thermoelectric cooling/heating ( $\alpha$ ,  $I$ ,  $T_c$  or  $T_h$  stand for the Seebeck coefficient, electrical current and temperature of the cold/hot junction respectively), and the second term represents heat transfer between two junctions ( $k$ ,  $\Delta T$  stand for thermal conductance of the thermoelectric pellets and temperature difference between two junctions respectively). Lastly, the third term indicates Joule heating and its sign convention varies according to the cooling/heating mode.

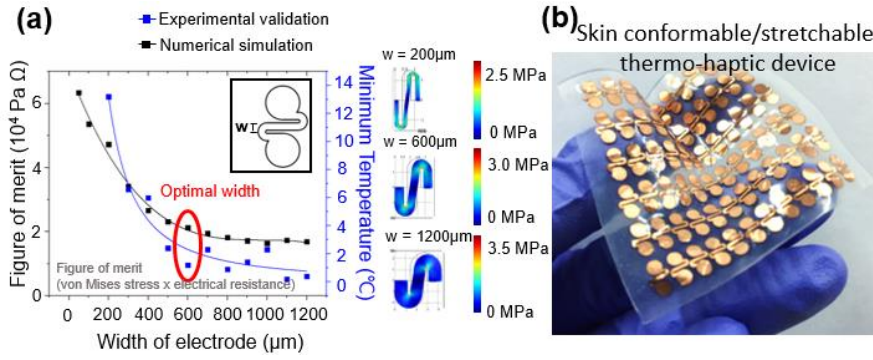


**Figure 3.2: Determining the interconnecting electrode geometry** (a) Schematic illustration of device bi-functionality, which can both cool/heat the body surface with the single device by simply changing the direction of current. (b) Numerical simulation and experimental validation to determine the Cu serpentine electrode specification by optimizing electrical conductivity and mechanical stress under 50% strain. The inset represents a product of numerically calculated von Mises stress and electrical resistance, and the blue plot signifies minimum temperature that the device attained at the corresponding width of the Cu serpentine electrode. Also, visually representation stress distribution for different size of electrode width under 50% strain. (c) Photograph of the Cu serpentine electrode encapsulated with Ecoflex.

To take account of both cooling capacity and mechanical strength, the width of Cu electrode was determined by comparing the figure of merit that considers both electrical resistance and von Mises stress when strain was set as 50% with the thickness of the Cu serpentine electrode fixed at  $25\mu\text{m}$ . The figure of merit was defined as a product of electrical resistance and von Mises stress, implying that the smaller values of figure of merit are more likely the electrode exhibit higher cooling capacity and mechanical robustness. The result shows that the figure of merit reaches its local maximum at  $w = 200\mu\text{m}$ , and it started to decrease with the width smaller or larger than  $w=200 \mu\text{m}$ . **Figure 3.3** presents separate electrical resistance and von Mises stress values at various Cu serpentine electrode width, and it can be observed that the electrical resistance is relatively high while von Mises stress was low at  $w=100 \mu\text{m}$ , which makes it undesirable for the electrode design. In order to determine the Cu electrode width at  $w \geq 300\mu\text{m}$ , a unit-cell was assembled with various Cu serpentine electrode width and examined minimum temperature generated by applying 2.0 A as in **Figure 2a**. The result shows that electrical resistance becomes a limiting factor for cooling, and thus temperature difference of

samples with width 300~400  $\mu\text{m}$  deviates from that of samples with larger width. The experimental result correlates with electrical resistance numerical simulation in which electrical resistance begins to converge from  $w=500\mu\text{m}$ . Considering the trade-off between electrical and mechanical properties with various width, 600 $\mu\text{m}$  was determined as an optimal width of the Cu electrode as in **Figure 3.2b**.

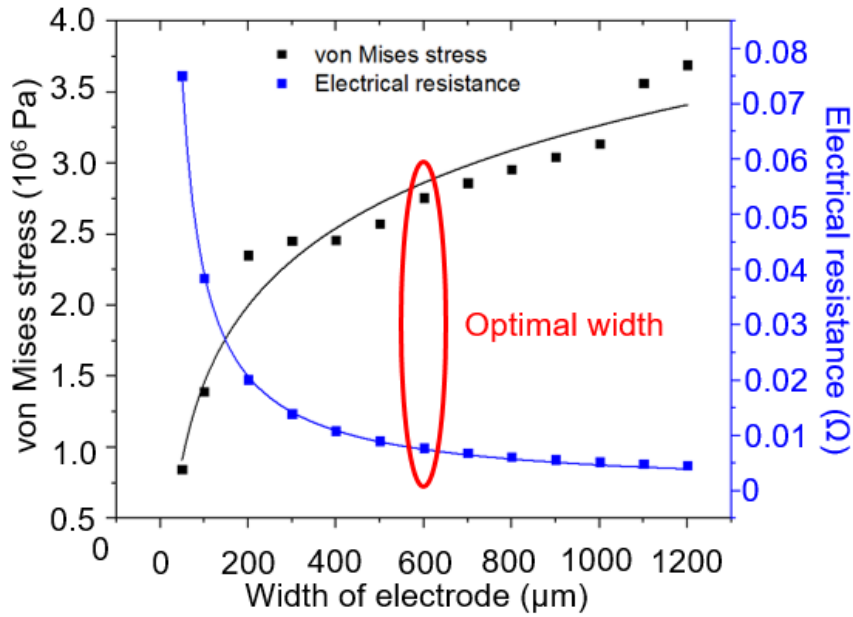


**Figure 3.3.** Numerical calculation of von Mises stress and electrical resistance with stretchable Cu electrode width at the strain of 50%.

Also, the numerical simulation was conducted on the various thickness and validated the design with experimental results, because the thickness of the electrode is another parameter that plays an essential role in the Cu electrode design. Please note that  $t=15\mu\text{m}$ ,  $t=25\mu\text{m}$  (current design) and  $t=50\mu\text{m}$  are the off-the-shelf copper foil products. **Figure 3.4a** shows the figures of merit of all thicknesses that generally follow a similar pattern with an inverse relationship with the electrode width and flattening as the electrode width increases. This is mainly because electrical resistance experiences an exponential decay while the mechanical stress exhibits a rather gradual rise with increasing electrode width. The numerical simulation result suggests that although  $t=50\mu\text{m}$  demonstrates the highest

figure of merit in terms of electrical conductivity and mechanical robustness, experimental validation is still needed to determine the optimal thickness of the Cu electrode because the difference among three conditions appears to be quite small.

Therefore, in order to validate the result of numerical simulation, minimum achievable temperature of the unit-cell was measured as well (a single n-type and p-type pellet) that has varying width and thickness of the electrode at 2.0A as in **Figure 3.4d** (Please note that some points with narrower width are missing, due to technical difficulty in fabrication). The result demonstrates that the cooling capacity with  $t=15\mu\text{m}$  is generally weaker than that the other two other electrodes, mainly because electrical resistance became a limiting factor for most conditions with  $t=15\mu\text{m}$ . On the other hand, graphs of  $t=25\mu\text{m}$  and  $t=50\mu\text{m}$  exhibit similar minimum achievable temperature with a minor discrepancy, indicating that above a certain point electrical resistance is not a limiting factor any longer. Thus, considering that the two conditions ( $t=25\mu\text{m}$  and  $t=50\mu\text{m}$ ) demonstrate comparable cooling capacity as in **Figure 3.4d**, it is rational to choose thinner ( $t=25\mu\text{m}$ ) as the optimal Cu electrode thickness, because often a thicker metallic electrode experiences higher mechanical stress when strained, which is also illustrated in **Figure 3.4b**.

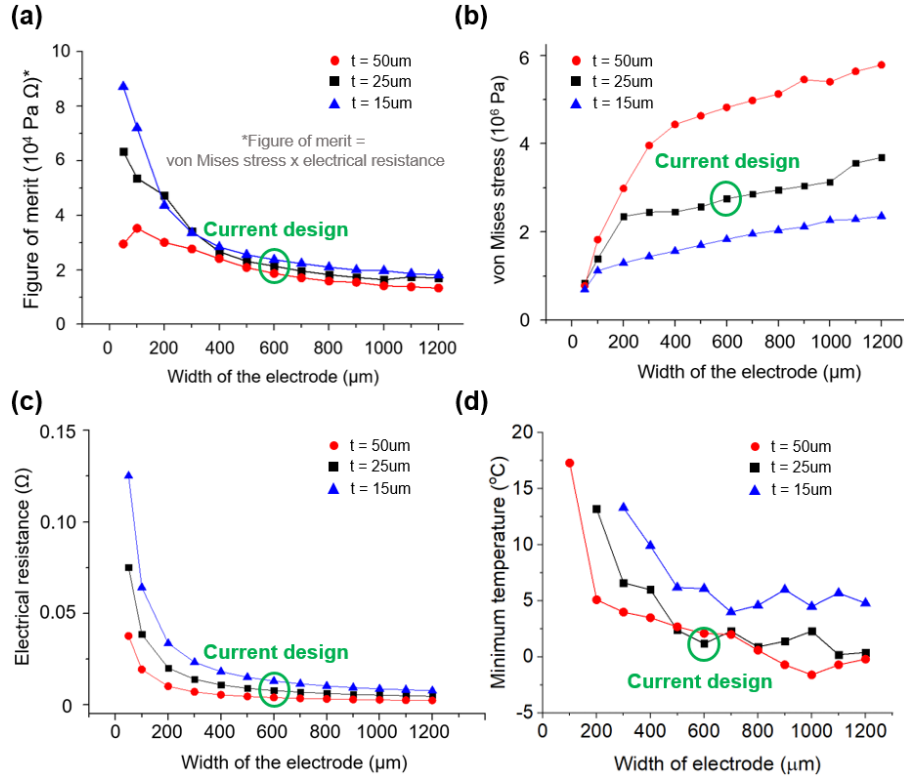


**Fig. 3.4:** Numerical simulation and experimental validation for optimization of the Cu electrode. (a) a figure of merit (b) von Mises stress and (c) electrical resistance with varying width and thickness of the electrode. (d) Experimental validation of varying thickness and width of the electrode. Please note that some points in the electrode width of 50μm, 100μm, and 200μm are missing, because they are too thin to fabricate.

### 3.3. Optimizing the design parameters of thermoelectric semiconductor pellets

Along with determining the design parameters of the serpentine electrode, material selection and examining the geometric effect of the thermoelectric pellet serve to affect the performance of the thermoelectric performance as well.  $\text{Bi}_2\text{Te}_3$  alloy was selected for both n-type and p-type materials because they exhibit higher  $zT$  (figure of merit) values at room temperature than many other candidates as can be seen in **Figure 3.5a** and **b**.<sup>[29]</sup> The working temperature of the thermo-haptic device ranges must lie within the temperature that causes pain or epidermal tissue damage, and this temperature window corresponds a range from 15  $^{\circ}\text{C}$  to 45  $^{\circ}\text{C}$ .<sup>[23]</sup> For this reason,  $\text{Bi}_2\text{Te}_3$  alloys are considered to be the most promising thermoelectric material to date at low-temperature applications such as this work.

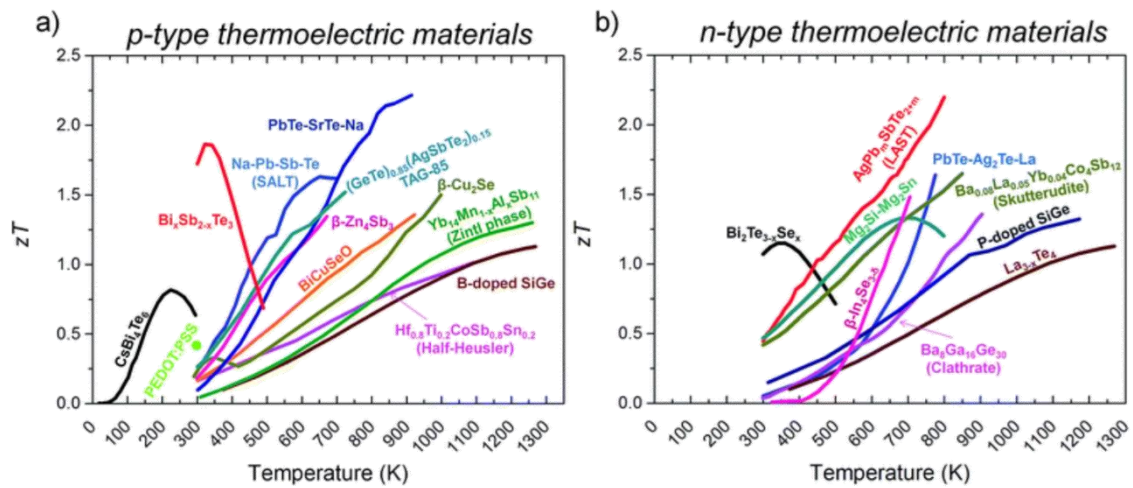


**Fig. 3.5:** The effect of temperature on figure of merit of p-type and n-type thermoelectric materials

1.4mm x 1.4mm x 1.7mm pellet was used as the current design out of other off-the-shelf products with different dimension after theoretical consideration by conducting numerical simulation with identical material properties and device architecture as in **Figure 3.6a**, which is used to theoretically calculate maximum  $\Delta T$  of the device with different pellet dimension. First, the overall size of the pellets was compared with other off-the-shelf products with different size (please refer to **Figure 3.6b**) at various current. **Figure 3.6c** indicates that the current design achieves the highest  $\Delta T$  among all samples possibly due to two reasons: the larger pellet dimension causes the electrical resistance to rise, and the smaller dimension results higher heat transfer from the hot junction of the device.

Furthermore, with  $l$  and  $w$  set as 1.4mm, the height of the pellet was changed to determine if there is an optimal height, and the numerical simulation implies that the moderate height (current design) produces the similar performance as the tall pellet as in **Figure 3.6d**. On the other hand, the small pellet exhibited rather lower performance, perhaps because the reduction in the height of the pellet to a certain degree results in increased heat conduction from the hot junction. Considering that performance of the

current design and the tall pellet does not differ much, it is reasonable to select the pellet with the lower height (current design), because the complete device with taller pellets would cause a higher degree of rigidity, which is not desirable for the device design in this work.

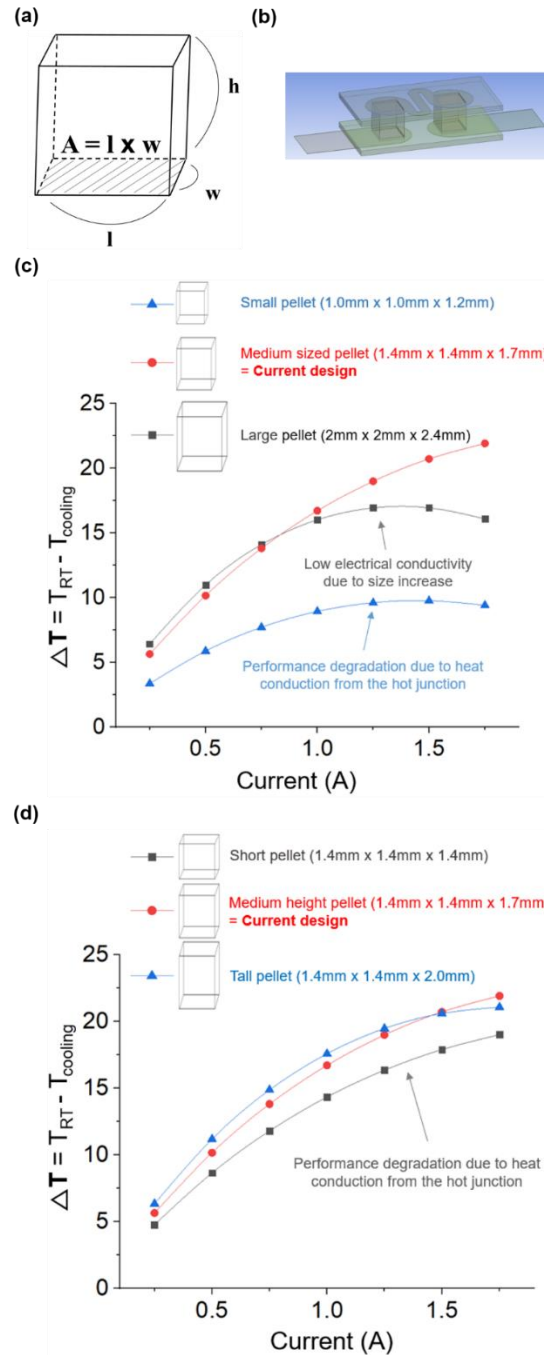


**Figure 3.6:** Design parameters of the thermo-haptic device. The dependency of the device performance upon (a) various pellet size and (b) height. (c) Schematic of the pellet dimension. (d) Device architecture used in numerically simulating maximum  $\Delta T$  in pellet design.

### 3.4. Selective thermal engineering of the device architecture

Selective thermal engineering of the device architecture serves to enhance the cooling and heating capacity of the device. The device interior must consist of thermally insulating material in order to minimize the adverse heat transfer loss between each junction of the device, whereas its external surface should be highly thermally conductive to increase heat dissipation and heat flux of the device. **Figure 3.7** shows how various designs of the stretchable backbone affect overall performance and heat dissipation before the device is turned on and off at constant current of 2.0 A. **Figure 3.7a** presents a magnified view of the four different designs of devices and the corresponding schematic representations. Case I is comprised only of thermoelectric pellets interconnected by the serpentine Cu electrode, whereas Case II resembles Case I except that its skeletal structure is entirely immersed in Ecoflex. In contrary, Case III and IV encapsulates the serpentine Cu electrode with a thin film of Ecoflex and thermally conductive elastomer respectively. Ecoflex serves to mechanically retain the shape of the serpentine electrode under the extreme magnitude of strain.



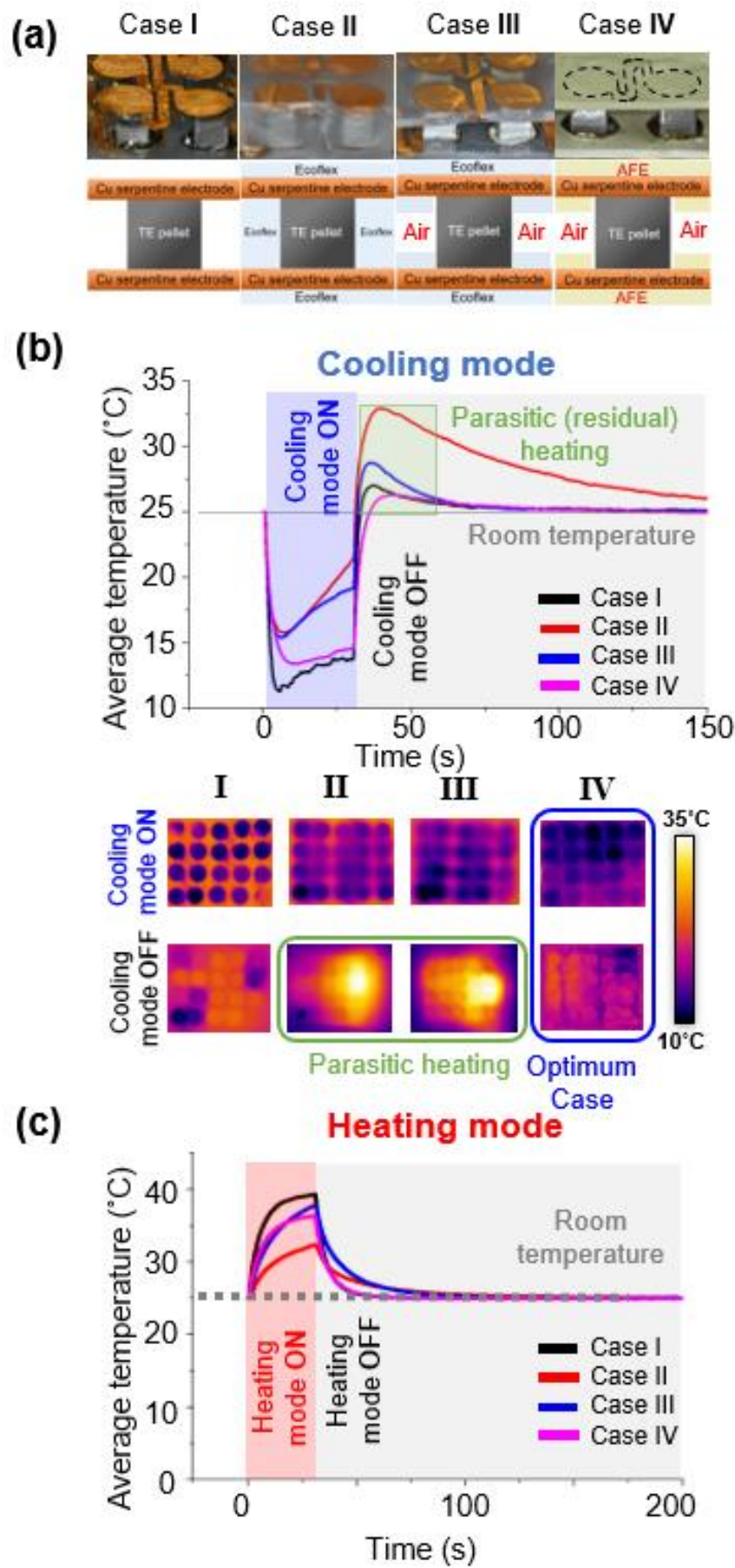


**Figure 3.7.** Selective thermal engineering of stretchable elastomer for device performance and heat dissipation enhancement demonstrated by time-dependent average temperature of different device designs when device is turned on and off. Case I is a bare skeletal structure composed only of thermoelectric pellets and interconnecting electrodes, whereas Case II consists of thermoelectric pellets and interconnecting electrodes, fully immersed in cured Ecoflex. Case III is comprised of thermoelectric pellets and electrodes, encapsulated with a thin layer of Ecoflex, and Case IV resembles Case III except that thermally conductive elastomer substitutes Ecoflex. Case IV corresponds to the final design of this report. (a) High resolution snapshots and schematic representations of Case I, II, III and IV architecture. (b) Time-dependent average temperature of Case I, II, III and IV. when the cooling mode is on and off. IR images shows temporal heat distribution of designs when the cooling mode is on and 10s after it is turned off. (c) Time-dependent average temperature of Case I, II, III and IV. when the heating mode is on and off.

Yet, the drawback of employing Ecoflex lies upon its relatively high thermal conductivity ( $0.2 \pm 0.01 \text{ W/m} \cdot \text{K}$ )<sup>[30]</sup>, which directly induces degradation of cooling and heating performance due to adverse conduction heat loss between both ends of thermoelectric junctions. When Ecoflex fills up vacant space as Case II,  $T_{\text{mean}}$  under the cooling mode only slightly drops to  $15.2^\circ\text{C}$  due to heat conductance from the hot junction via Ecoflex as in **Figure 3.7b**. In contrast, the absence of Ecoflex as in Case I extremely enhances the cooling capacity with  $T_{\text{mean}}$  of Case I reaching  $9.8^\circ\text{C}$  under the cooling mode, due to reduction of heat conduction from the other junction. Yet, without Ecoflex, the serpentine Cu electrode in Case I cannot return to its original shape once it is plastically deformed, since elastomer functions to mechanically support the electrode. Thus, in order to address this problem, both top and bottom surfaces of the Cu serpentine electrode were encapsulated with a thin layer of elastomer as in Case III and IV rather than completely filling the device interior, so that the elastomer executes its role to mechanically reinforce the electrode without performance degradation. As a result,  $T_{\text{mean}}$  of Case III and IV went down to  $12.9^\circ\text{C}$  and  $11.9^\circ\text{C}$  respectively after the cooling mode was turned on. Encapsulating the electrode with elastomer would fill the device interior with air insulation layer, and thus lower overall thermal conductivity of the device interior as in **Figure 3.8**, because air is one of the materials with the lowest thermal conductivity, therefore inhibiting heat transfer between each junction as a result.

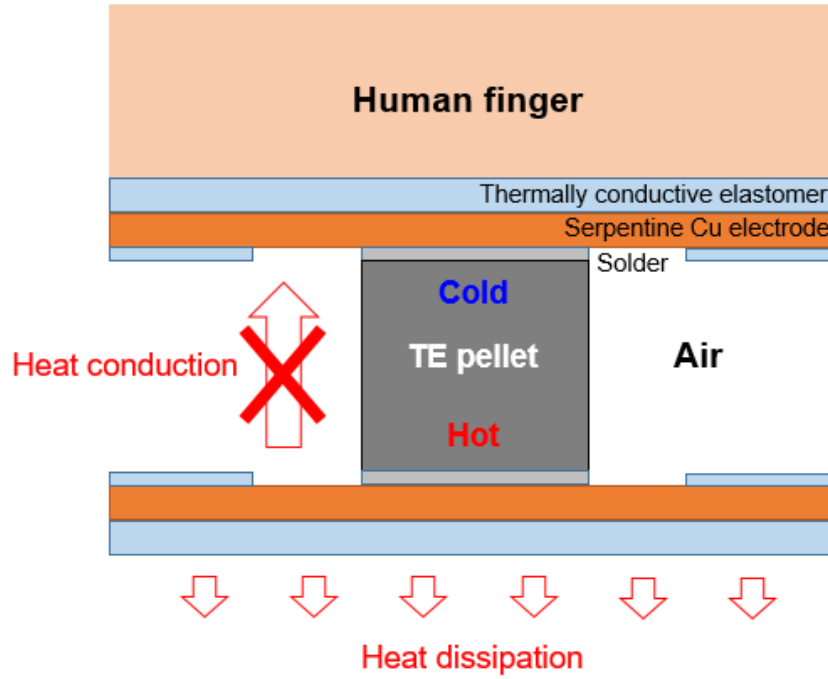


**Figure 3.8.** A simplified diagram of cross-sectional device structure and heat flow model when the cooling mode is turned on.

Compared to the thermally insulating device interior, the device exterior must be thermally conductive to remove heat generated by Joule heating and parasitic heat conduction from a heating side via thermoelectric pellets under the cooling mode. Yet, since the ultimate goal of this study is to fabricate a wearable thermo-haptic device, its exterior must remain highly stretchable.

For this reason, Ag flakes were incorporated into Ecoflex to boost its thermal conductivity while retaining stretchability of the device (Please refer to **Figure 3.9** and **3.10** for an extra explanation on mechanical properties of thermally conductive elastomer). The effect of employing AFE is apparent as in **Figure 3.8b**. Whereas  $T_{\text{mean}}$  of Case II and III steeply escalated,  $T_{\text{mean}}$  of Case IV was maintained to be constant when the cooling mode was continued for 30 s, implying that the thermally engineered structure of Case IV strengthens cooling capacity by removing heat to the outside the system.

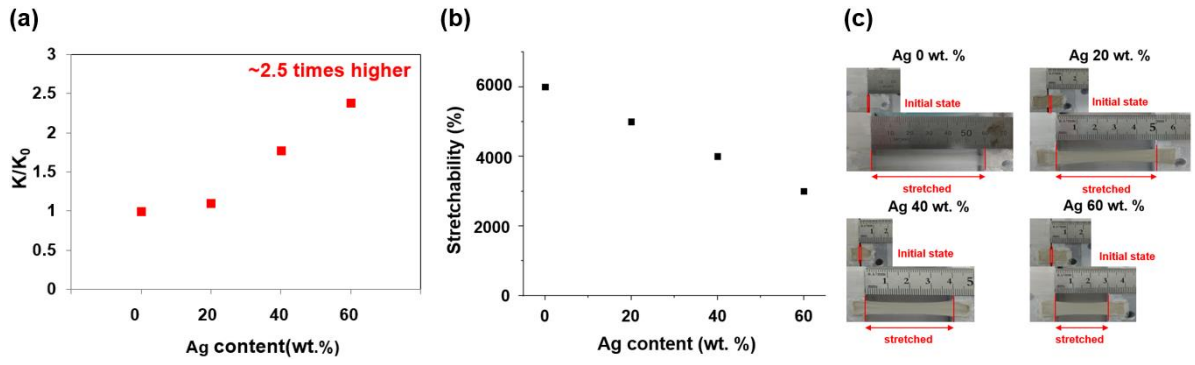


**Figure 3.9.** Thermal conductivity measurement and stretching test with varying Ag flake/Ecoflex ratio. (a) LFA thermal conductivity result (b) stretching test (c) photographic image of the set-up and samples

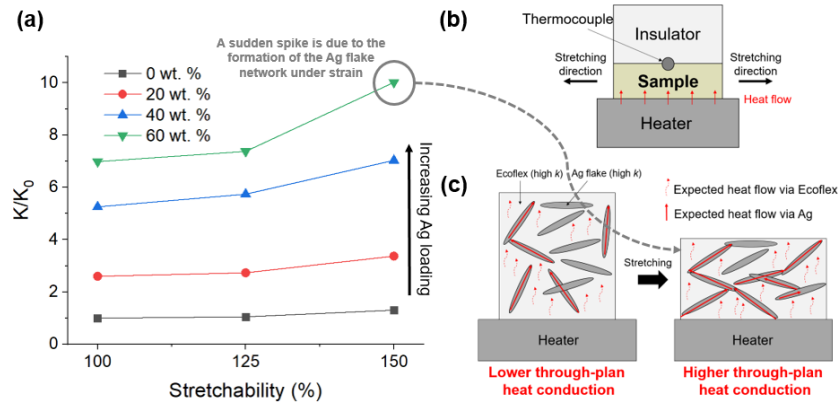


**Fig. 3.10:** Stretchability of the AFE with a various degree of stretchability. (a) graphical representation. (b) A schematic diagram of the experimental set-up. (c) Expected heat transfer when strained

Numerical simulation with identical material properties and device architecture as in **Figure 3.11** implies that the maximum achievable  $\Delta T$  of the current design theoretically goes up to 20.7 K for the cooling mode and the value does not greatly differ from the experimental data. Considering potential practical problems (such as voids in the solder, fabrication flaws, impurities and surface oxidation in materials), the discrepancy between calculated and experimental data appears to be quite reasonable).

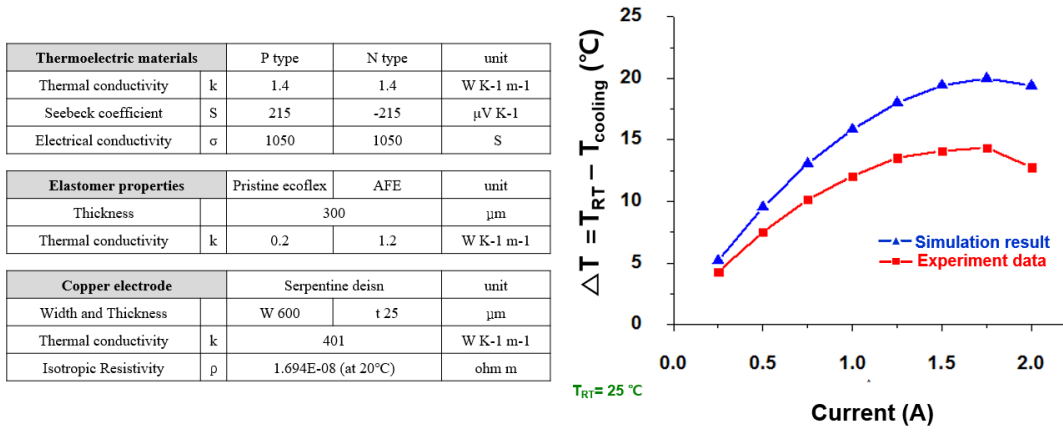


**Fig. 3.11:** Numerical simulation of the stretchable thermo-haptic device with identical material properties and geometric architecture. Comparison between experimental data and simulation result of minimum achievable temperature depending on varying temperature.

Another advantage of employing AFE lies on spreading heat in a lateral direction to maintain thermal uniformity under stretching as in **Figure 3.12**. Considering that the human epidermal tissue stretches by the maximum of 25%, the IR snapshots of stretched samples substantiates that AFE would manage to spread heat up to stretchability of 25%, therefore serving to reduce the trade-off between device coverage and stretchability.

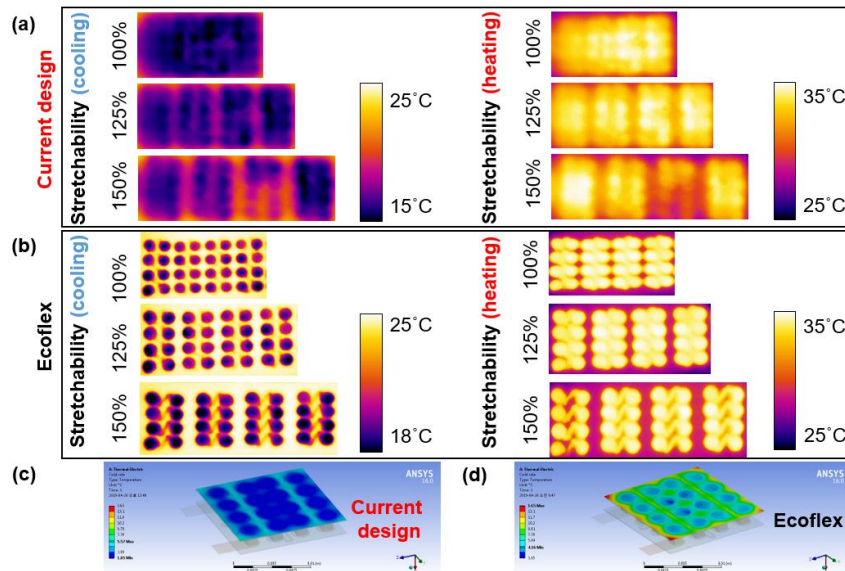


**Fig. 3.12:** IR snapshots of the device operation while stretched. (a) The cooling and heating mode of the current design under various degree of strain. (b) The cooling mode and heating mode of the sample using Ecoflex under various degree of strain. (c) Numerical simulation of the current design under the cooling mode. (d) Numerical simulation of the sample using Ecoflex under the cooling mode.

The effect of utilizing thermally conductive elastomer plays a much more crucial role under cooling mode after the current is turned off in terms of heat dissipation. Parasitic (residual) heat remains unremoved inside the device and starts to heat up the cold junction as in Case II and III in **Figure 3.8b**. This phenomenon is visually represented in the IR camera images inside a green box, which is taken 10s after current is turned off.  $T_{\text{mean}}$  of Case II and III rises to 32.1 °C and 28.7 °C respectively when it is supposed to approach room temperature: a highly undesirable effect for thermo-haptic system because this parasitic heat may evoke a false thermal sensation on a human epidermis. On the other hand, optimum design (case IV) immediately returns to room-temperature after current is turned off, because its thermally conductive exterior serves to promote heat exchange with the environment to the great extent. Likewise, IR images of Case IV (marked in a blue box) appear to be free of parasitic heat generation 10s after current is turned off, indicating that the heat dissipation of Case IV matches that of Case I, which is the most ideal case in this study, when current is both turned on and off.

The selective thermal engineered design exerts a favorable effect on the heating mode as well. In **Figure 3.7c**,  $T_{\text{mean}}$  of Case II was lower than Case I, III and IV at 0.6A when the heating mode was on, due to the greater loading and specific heat of Ecoflex, requiring more energy to heat up the entire system. It must be noted that the heating capacity of Case III was a slightly higher than that of Case IV unlike in the cooling mode, because thermally conductive elastomer of Case IV serves to exchange heat to the surrounding, marginally lowering its heating capacity. However, after the heating mode is turned off, it took much longer time for Case II and III to return to room temperature than Case IV. Just as in the cooling mode, AFE in Case IV enhances heat exchange with surrounding, and it could be observed that  $T_{\text{mean}}$  of Case IV so rapidly approaches room temperature

that its decaying rate almost overlaps with that of Case I, the ideal model in this report.

Another role of incorporating AFE on the device exterior is to improve heat transfer between a human body surface and the device. A high heat transfer rate between human epidermis and the device requires a highly thermal conductive material, since heat flux is a direct function of thermal conductivity. Therefore, applying AFE on the device surface where heat transfer occurs is expected to further enhance its cooling and heating performance. Furthermore, the absolute value of heat flux of Case IV is much higher than that of Case II and III and the closest to that of Case I, indicating that thermally conductive elastomer improves heat transfer at the human body/device interface.

## **Chapter 4**

### **Characterization and performance evaluation of the device**

#### **4.1. Cooling and heating performance of stretchable thermo-haptic device**

Various characterization tests conducted herein present a cooling and heating characteristics of the thermo-haptic device that is highly differentiated from other coolers and heaters reported so far. Unlike reported coolers or heaters, the device exploits the highly advantageous properties of thermoelectric effect that can actively generate a discrete magnitude of both cooling and heating with the single device by applying a various amount of current. **Figure 4.1** shows time dependent temperature profiles of both cooling and heating mode along with the corresponding IR temperature distribution image at increasing current with the time interval of 20s. Apparently, the calibrated amount of current was applied to induce equivalent temperature change for cooling mode and heating mode to take account of the inherent Joule heating effect in cooling mode. The result suggests that applying an arbitrary amount of current as an input to the device

produces desirable temperature for both cooling and heating in a very short amount of time, exhibiting a highly controllable thermal profile and bi-functional nature of the single device.

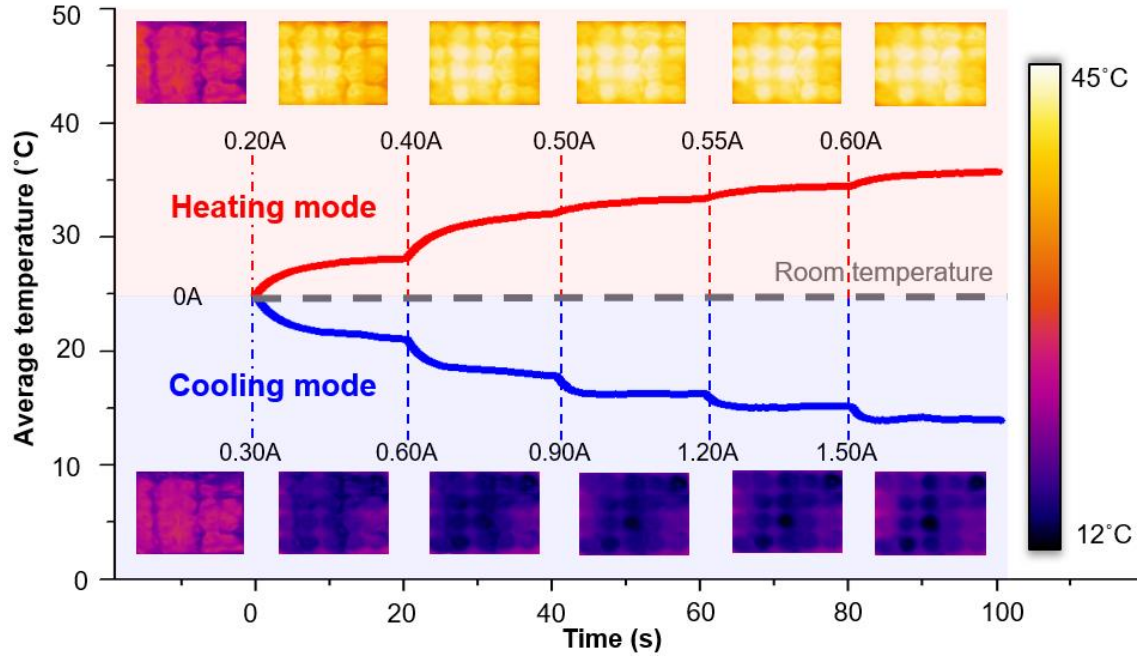


**Figure 4.1 | Cooling and heating mode characterization and active temperature control of the stretchable thermo-haptic device. (a)** Temperature evolution and corresponding IR camera images of cooling and heating mode at the stepwise current increase.

Various characterization tests conducted herein present a unique cooling and heating characteristics of the STH device. Unlike reported coolers or heaters, the device exploits the highly advantageous properties of the thermoelectric effect that can actively generate a discrete magnitude of both cooling and heating with the single device by controlling the electrical signal. **Figure 4.1** shows time-dependent temperature profiles of both cooling and heating mode along with the corresponding IR temperature distribution image at increasing current with a given time interval. The result suggests that the device produces desirable temperature for both cooling and heating in a very short time, exhibiting a very fast and highly controllable thermal profile and bi-functional nature of the single device.



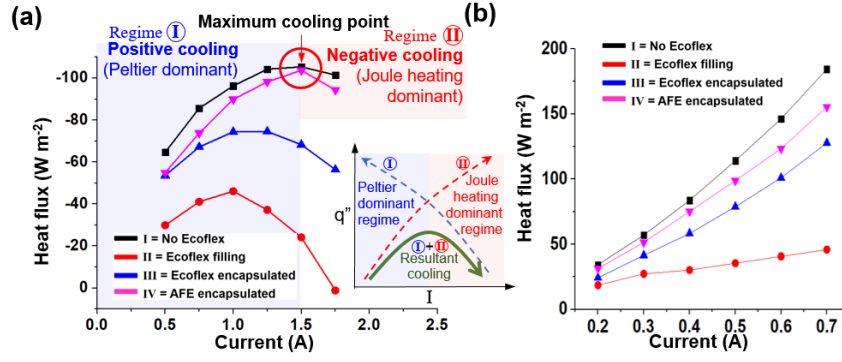


**Figure 4.2:** (a) Heat flux measurement of different device designs under the cooling mode. Note that cooling mode is a sum of two competing regimes (positive cooling (Peltier dominant regime) and negative cooling (Joule heating regime)) and shows maximum efficiency at 1.5A followed by decrease with increasing current. (b) Heat flux measurement of different device designs under the heating mode. Note that heating mode shows monotonic increase with applied current.

Moreover, to examine cooling and heating capacity, heat flux was measured at a various range of current for the cooling and heating mode with a commercial thin-film heat flux sensor as in **Figure 4.2b** and **c**. The heat flux of the cooling mode shows an initial increase and a maximum heat flux at 1.5 A followed by a decrease with increasing current while that of heating mode shows a monotonic increase with increasing current. This difference originates from the two inherent competing regimes in cooling mode; (I) positive cooling in Peltier cooling dominant regime (blue shaded box in **Figure 4.2b**) and (II) negative cooling (=heating) in Joule heating dominant regime (red shaded box in **Figure 4.2b**). The resultant heat flux (green line in **Figure 4.2b**) inset) in cooling mode is the sum of these two competing modes because the heat generated by Joule heating counteracts the cooling effect in cooling mode. Therefore, heat flux of Case IV gradually increased up to 1.5 A (positive cooling), which is equivalent to the maximum point, and it started to decrease at current larger than 1.5 A (negative cooling), making the cooling mode much more challenging than the heating mode. Furthermore, heat flux of this device was compared to that of the commercial rigid device for both cooling and heating modes, and **Figure 4.3** demonstrated only a reasonable difference in device capacity. The figure

suggests that the commercial device exhibits the cooling and heating capacity that are roughly 2.5 times and 1.8 times higher than the device respectively. The difference in performance between two devices mainly stems from thermal conductivity difference of the supporting substrate and fabrication flaws. The commercial thermoelectric module uses a ceramic plate as a substrate, which has much higher thermal conductivity than that of AFE. Moreover, the automated and precise process is employed to fabricate commercial products, whereas the fabrication process used herein often incurs human error. Thus, considering the factors mentioned above, the discrepancy in the device performance between the commercial thermoelectric module and stretchable thermo-haptic device appears to be highly reasonable.

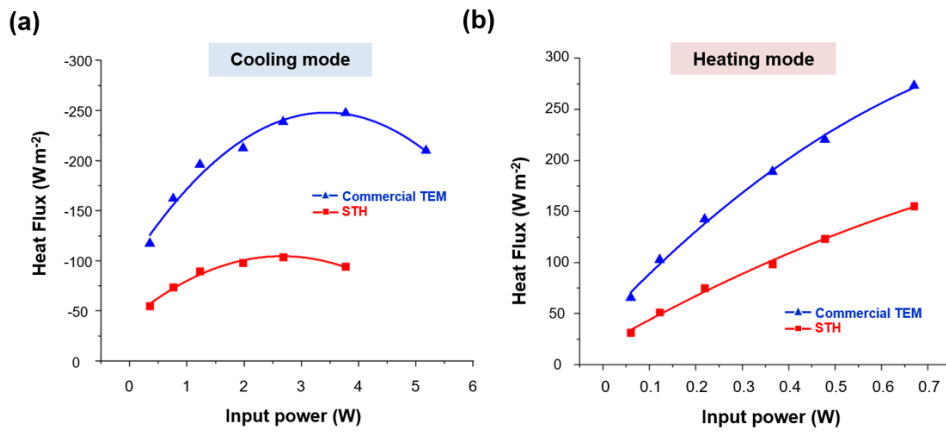


**Fig. 4.3:** Comparison of heat flux between stretchable thermo-haptic device and commercial thermoelectric module of (a) the cooling mode and (b) the heating mode.

#### 4.2. Reversed mode for accurate and desirable thermal sensation

One of the major problems of previous coolers or heaters to be utilized in wearable electronics and ultimately in VR application is that they mainly depend on natural convection which is a very slow heat transfer mode and thus usually take much longer time for the device temperature to change. However, the stretchable thermo-haptic device

can actively cool down or heat up by applying inverse voltage with the single device. Thus after the desired temperature is attained, it can revert to room-temperature much faster than other coolers or heaters, enabling accurate control of thermal sensations. **Figure 4.4a** and **b** compares time it takes to return to room-temperature with ( $\tau_{\text{reversed}}$ ) and without ( $\tau_{\text{natural convection}}$ ) under the cooling and heating mode, and the result is dramatic. The target  $\Delta T$  was set as 15 K and measured time  $\tau_{\text{reverse}}$  and  $\tau_{\text{natural convection}}$  within an error of 1% with an IR camera. The result demonstrated that the reverse modes under heating and cooling were 9.59 times ( $\tau_{\text{reverse}} = 3.52$  s and  $\tau_{\text{natural convection}} = 33.76$  s) and 9.42 times ( $\tau_{\text{reverse}} = 4.48$  s and  $\tau_{\text{natural convection}} = 42.24$  s) faster respectively than single-mode natural convection or conduction.

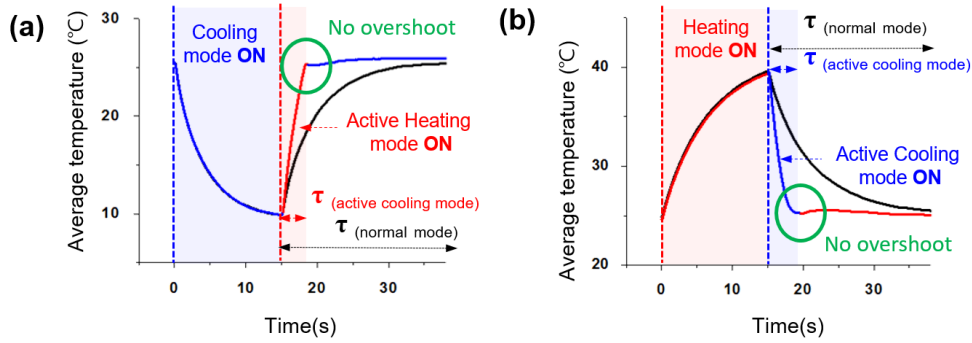


**Figure 4.4:** (a) Comparison between the reverse mode (active heating) and normal mode to return to room temperature after cooling mode is off. (b) Comparison between the reverse mode (active cooling) and normal mode to return to room temperature after heating. Note that the temperature response much faster in an active control mode. Reverse modes were carried out by applying inverse current after cooling and heating respectively. Also, varying the magnitude of current in the course of reversed mode eliminates the overshoot.

Furthermore, note that gradual controlling (high to low) the magnitude of current in the course of the reversed mode eliminates the temperature overshoot, which has been present in **Figure 4.5**. The larger magnitude of applied current causes the tighter alignment of charged carriers (holes and electrons) inside the thermoelectric pellet, requiring a longer

time for the charged carriers to diffuse randomly throughout the pellet. Thus, the magnitude of current was varied in the course of the reversed mode gradually from the high to low magnitude to loosen the alignment toward the end of the reversed mode. As a result, the overshoot is no longer present, and the reversed mode directly approaches room-temperature for both cooling and heating mode as in **Figure S11b**.

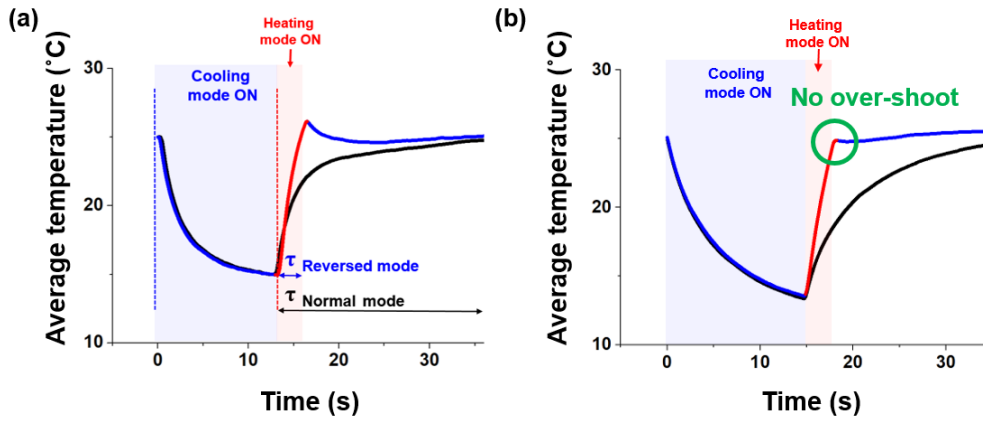


**Figure 4.5.** Comparison of reversed mode (a) with and (b) without over-shoot. Constant current was used for the reversed mode in (a) whereas varying current (high to low) was used in (b).

**Figure 4.6** depicts the cyclic test with reversed modes overlapped with normal cooling and heating mode. Since the device utilizes the reversed mode to generate the temperature difference unlike other reported heaters or coolers that rely only upon natural convection, almost 3 cycles can be realized with both reversed modes when only one cycle can be attained with the normal mode. This characteristic to express temperature change in a much higher frequency empowers the device to strategically mimic much more accurate and diverse virtual situations for its potential use.

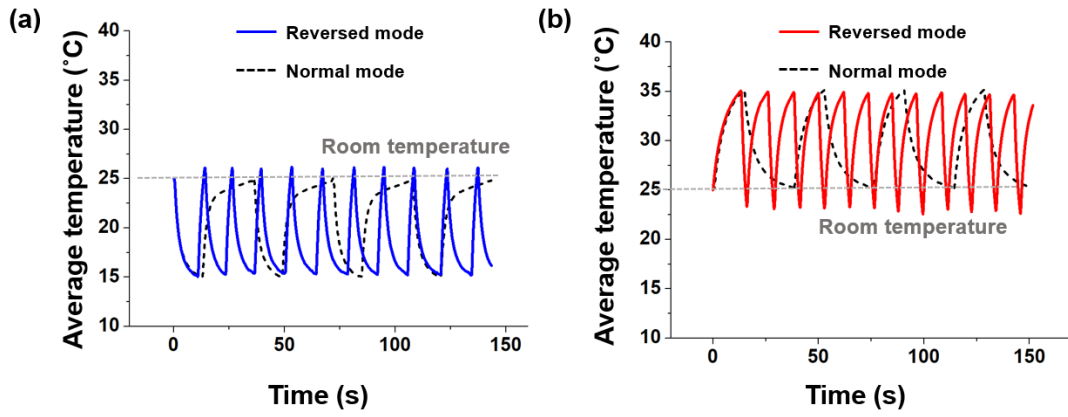


**Figure 4.6:** Overlapped presentation of reversed and normal mode in cycles under (a) cooling and (b) heating modes.  $\Delta T$  was set as 10K for both cooling and heating.

### 4.3. Mechanical robustness of the device against various stress

For the device proposed in this report to be fully wearable, the high mechanical robustness and durability while maintaining device performance are a crux issue. Various mechanical deformations constitute external quotidian stress, and therefore a variety of mechanical stress to the device was varied to validate its wearability. **Figure 4.7a** shows that the device can stretch up to 230% without degradation in both cooling and heating capacity since stress is mostly distributed at Ecoflex and a serpentine electrode region, which either possesses relatively lower Young's modulus or is designed to deform structurally (**Figure 4.8** provides the IR snapshots of the operating device while stretching up to 230%).

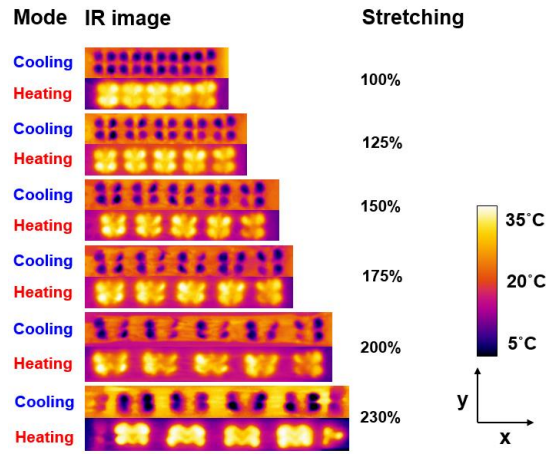


**Figure 4.8** IR camera image of cooling and heating mode while stretching. Ecoflex was used instead of AFE in this experiment to determine the cause of the mechanical failure under maximum stretching.

The cyclic stretching test as in **Figure 4.7b**, on the other hand, demonstrates the contribution of the structural electrode design to withstanding high fatigue stress, which is most likely to cause mechanical failure in wearable electronics. Considering human epidermis can experience stretches by 25% maximum, strain was limited in cyclic stretching test to 50%, and the result substantiates the cyclic durability of the device. The result demonstrates that the device could withstand severe fatigue stress without significant performance degradation even after  $1.4 \times 10^4$  cycles as in the inset. To evaluate the mechanical stability of the device against potential everyday stress, the device was attached to the palm and measured electrical resistance change while repeatedly folding and unfolding the hand as in **Figure 4.7c**. The result shows that the resistance change fluctuation fell under a range of  $R/R_0 < 25\%$  and returned to the original value in the absence of stress, validating the mechanical robustness of the device against quotidian stress.

Thermal stress was examined by repeatedly alternating the cooling and heating modes with  $\Delta T = 15^\circ\text{C}$  as in **Figure 4.7d**. The thermal mismatch at material interfaces might

cause thermal stress on the device, possibly leading to an electrical breakdown of the entire system due to a rapid temperature change when operated in a large number of cycles. Yet, the device remained fully operational over 5,000 s without major performance degradation, substantiating the overall mechanical durability of the device and its potential to be employed in the wearable application.

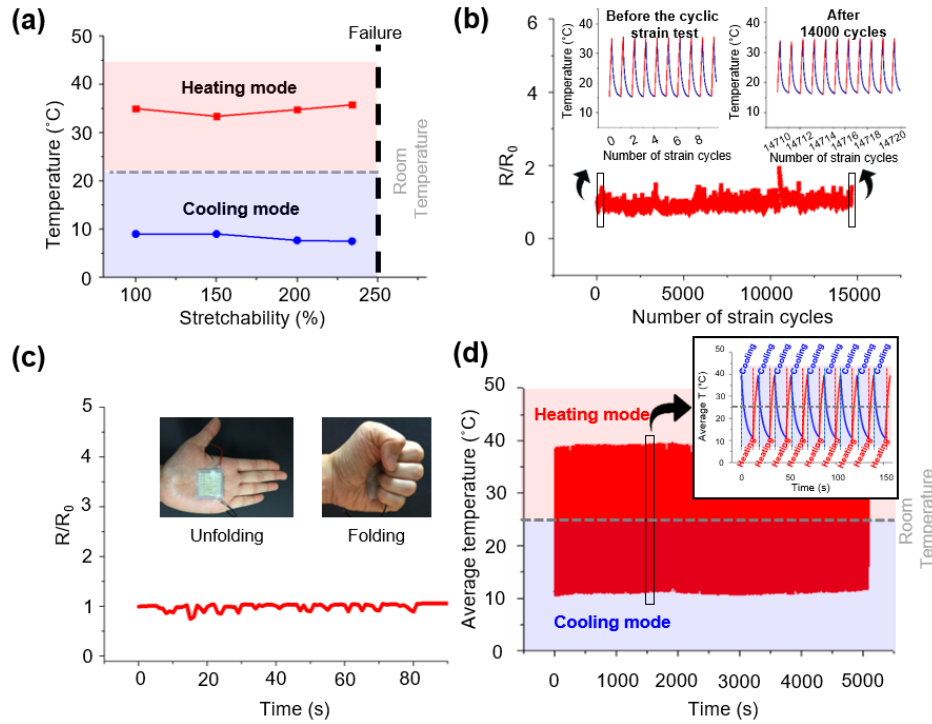


**Figure 4.7:** (a) Step-wise increasing and maximum strain applied to the device while retaining cooling/heating capacity. (b) Resistance change during a cyclic test in which a cycle consists of applying 50% strain and releasing it. (c) Resistance change of the stretchable thermo-haptic device when folding and unfolding the hand for 11 times. (d) Cyclic temperature profile in which cooling and heating alternated.  $\Delta T$  was set as 10K. The inset shows a magnified view of alternating cooling and heating cycles.

## Chapter 5

### Wearable personal thermal management

#### 5. Examining the device potential to for wearable personal thermal management

Exploiting the strengths of the device reported herein, the practical applications were

presented such as personal thermal management and a wearable thermo-haptic VR system. As the device can stretch and attach to a curved surface, it can be conformably affixed to any part of the soft human body. Moreover, the bio-compatibility of Ecoflex and Ag flake makes it a suitable candidate for wearable electronics applications.<sup>[31]</sup> **Figure 5.1a-c** illustrates a cooling and heating temperature profile of hand-shaped PDMS (polydimethylsiloxane) with a 27 mm x 27 mm STH device, recorded in-situ with the IR camera to examine its potential usage in personal thermal management (Refer to **Figure 5.2** for the experimental setup). Localized cooling and heating show that the temperature difference is approximately 13 K for both as in **Figure 5c**, suggesting that both cooling and heating performance are effective enough to provoke both feelings of cold and warm.

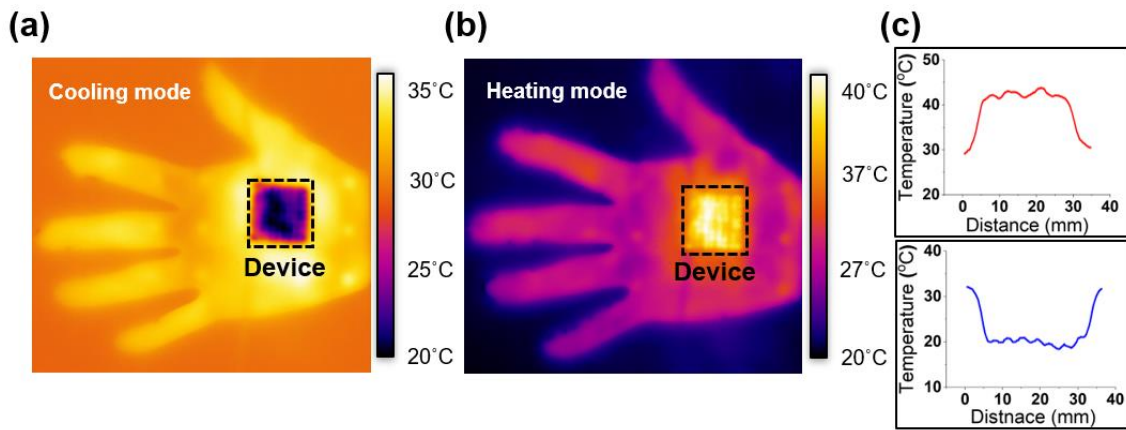


**Figure 5.1:** (a) Localized cooling of 1 mm thick hand-shaped PDMS at 1.5A (b) Localized heating of the hand-shaped PDMS at 0.65A. (c) Graphical representation of temperature difference between cooled/heated area and surrounding of the hand-shaped PDMS



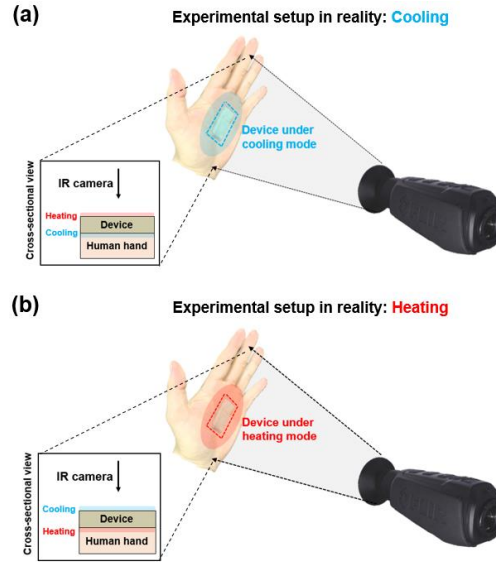


**Fig. 5.2:** An experimental setup coupled with IR view of (a) the cooling and (b) heating mode on hand. Note that the cooling mode of the device appears as if it is heating the hand and the same applies to the heating mode.

## Chapter 6

### Reconstruction of artificial thermal feeling with the stretchable thermo-haptic device in VR space

#### 6.1. Integration of device to the finger motion tracking glove

To evaluate the diverse applicability of the STH in wearable VR applications, wearable heat-sinks were attached to the three independent devices and integrated with the previously developed finger-motion tracking glove<sup>[28]</sup> as in **Figure 6.1** with the PID controlled system (**Figure 6.2** represents the simplified illustration of the electric circuit of the whole feedback hardware system) to replicate real-life virtual situations, recorded with a digital camera, a virtual display and thermocouple respectively as in **Figure 6.3**.



**Figure 6.1:** The photographs of the palm and back side of VR glove, consisted of thermo-haptic devices and finger-motion tracking module.

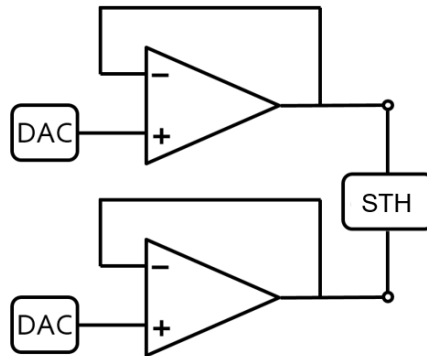


**Figure 6.2:** A simplified electrical circuit illustration comprised of DAC, op amplifier and STH

## 6.2. Replicating the thermal sensation of virtual objects at various temperature

**Figure 6.3** demonstrates in-situ data collection of temperature in a virtually realized scenario in which the user touches objects at different temperature such as a cold beer bottle, a chilly soda bottle, a mug of warm green tea and a mug of hot coffee (from left to right in **Figure 6.3** bottom inset pictures). It shows that the PID-controlled STH closely reproduces the temperature change of objects. The PID control simultaneously calculates the error value from the set-point and enters a correction according to the mathematical algorithm to approach the set-point, constituting a control loop feedback mechanism.

**Figure 6.4** includes varying voltage signals over time, based on the algorithm to meet the

target temperature for all virtual scenarios in **Figure 6.3**. As a result, STH reached the target temperature of various virtual actions shortly after the contact and held the target temperature with only small fluctuation due to the PID control during the contact with the object, creating thermal conditions analogous to the real-life situations. Another fascinating feature of our thermo-haptic device module occurs when fingers are detached from the objects. Using the reverse mode of STH, the temperature rapidly approaches room-temperature after touching both cold and warm objects. The reverse mode provides accurate thermal sensation and eliminates the unintended thermal residue, whereas other reported single-mode heater or cooler would suffer from an undesirable thermal trace until natural convection completely removes it, ultimately evoking false thermal sensation.

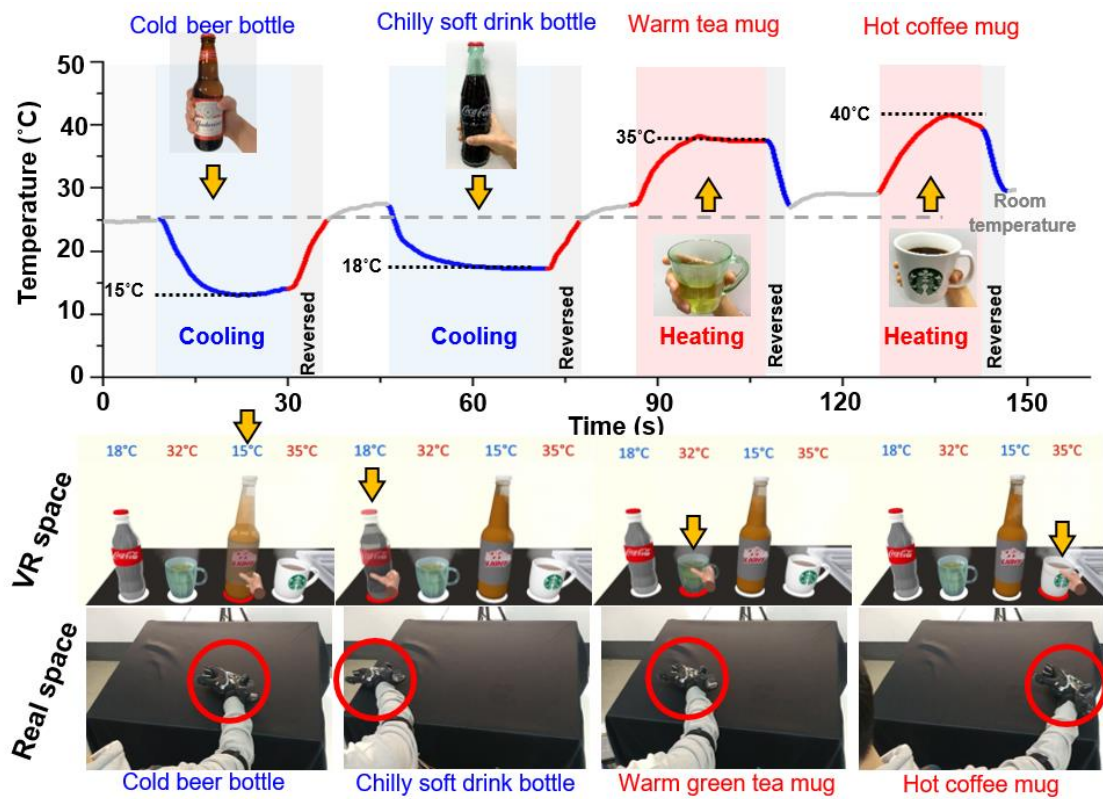


**Figure 6.3:** (a) Reproducing virtual situation of touching objects at various temperature. The graph shows temperature change based upon the virtual scenario of touching various objects. The two sets of snapshots correspond to the simultaneous motion of the hand in VR display and real life respectively.

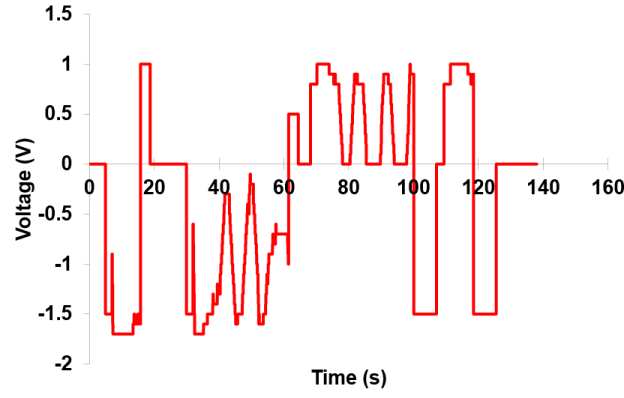


**Figure 6.4:** Transient voltage output signals that change based upon the mathematical algorithm and target temperature.

In addition, three STH devices affixed to different fingertips come in contact with a soda bottle at 18 °C (left graph) and a mug of green tea at 32 °C (right graph) one at a time as in **Figure 6.5** to independent operation of devices, demonstrating that the individual STH device can be used to provoke a separate localized thermal sensation on each finger.

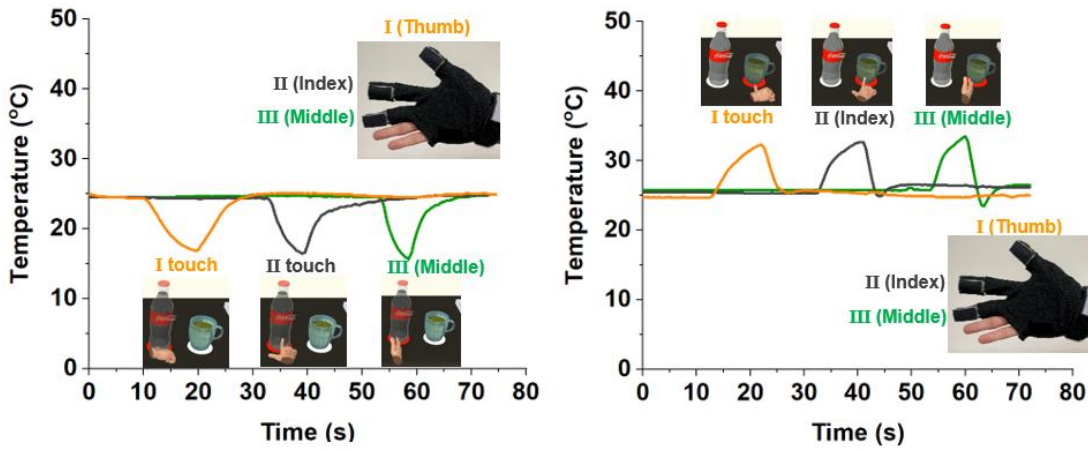


**Figure 6.5:** Cooling and heating of different fingers independent of each other, touching the soft drink bottle at 18°C and green tea mug at 32°C. The inset shows the corresponding fingers on the palm side of the proposed VR glove.

### 6.3. Replicating the thermal sensation of virtual objects with different thermal conductivities

As aforementioned, our skin is capable of distinguishing objects with different thermal properties at the same temperature. **Figure 6.6** compares the calculated temperature

change (left graph) and the simulated temperature change (right graph) by STH when touching materials of different thermal conductivity at the same temperature in a VR space. Using the equation<sup>[32]</sup>,  $\Delta T_{skin}$  were calculated and graphically represented when the user touches an object of given temperature.

$$T_{skin,s}(t) = \frac{-(T_{skin,i} - T_{object,i})(k_{skin}R)^2}{[1 + \frac{\sqrt{k\rho c}_{skin}}{\sqrt{k\rho c}_{object}}]} [1 - e^{\alpha_{skin} B^2 t} \text{erfc}(B\sqrt{\alpha_{skin} T})] + T_{skin,i}$$

where  $k$ ,  $\rho$ ,  $c$  and  $R$  are thermal conductivity, density, specific heat and thermal contact resistance respectively. As a result, the human skin undergoes a relatively steeper temperature drop when touching objects at 25 °C, while the virtually realized skin temperature does not fully follow the theoretical values and decreases rather slowly. Yet, it reaches the target temperature for all three conditions only with a few seconds of delays. The possible reason for the discrepancy originates from specific heat of AFE compared, and the device performance was expected to be enhanced in virtually realizing transient thermal conditions of objects with further accuracy if the thermal properties of the AFE are further improved in the future work.

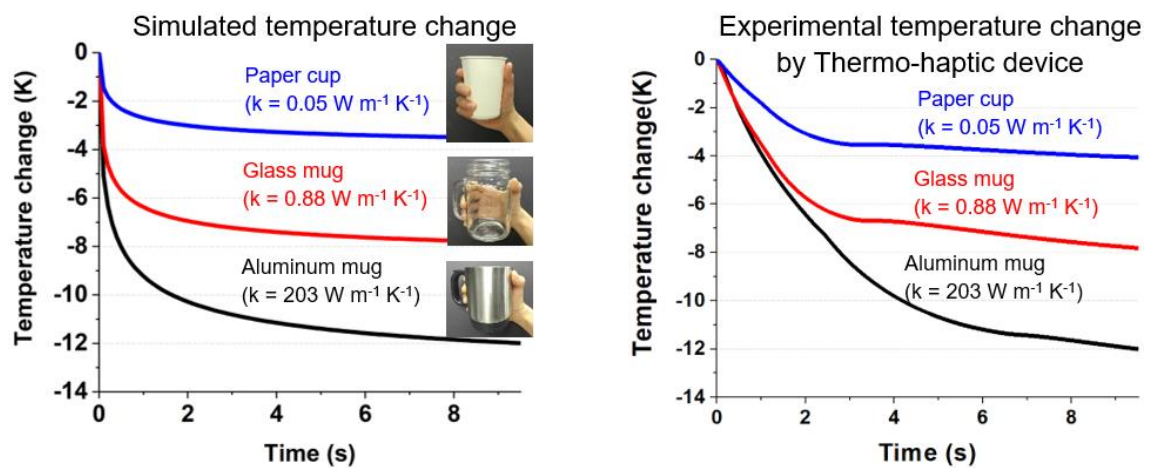


**Figure 6.6:** A comparison between theoretical and virtually realized values of the transient temperature of the hand, touching materials of different thermal conductivity at 25°C.

## **Chapter 6**

### **Conclusion**

In summary, the first demonstration of a skin-like, highly soft and stretchable and bi-functional (both cold and hot sensation) thermo-haptic device was presented for wearable VR applications, capable of simple switching cold and warm sensations by changing heat flux direction with a single device structure. The skin-like thermo-haptic device reproduces diverse thermal properties of objects on the skin in a virtual world with substantial accuracy and superior wearability. While most of the current haptic devices in the VR field are concentrated on the tactile sensation such as vibration, the developed thermo-haptic study shows that virtual sensation (artificial feeling) can be further integrated and augmented with thermal information. Due to its highly stretchable nature and rapid response rate, STH proposed herein can actively and yet discretely both heat-up or cool-down human body parts only in a few seconds with high controllability while stretching along with the bodily deformation. In addition, owing to the bi-functional nature and its unique reverse mode, STH can generate accurate and desirable thermal sensation with fast response, which meets the requirements to be utilized in VR applications. Integrated with the finger-motion tracking glove and the PID control, STH showed its potential feasibility to simulate various real-life thermal sensations in virtual space and thus is expected to further open up possibility for a next-generation haptic device to provide a unique thermal information for the more realistic virtual world field and thermal treatment in medical application field as well.

## References

- [1] Trainline Launches App Feature to Help Travellers Social Distance on Trains, Global Railway Review, 2 July 2020, [www.globalrailwayreview.com/news/103212/trainline-app-travellers-social-distance-trains/](http://www.globalrailwayreview.com/news/103212/trainline-app-travellers-social-distance-trains/).
- [2] Fortune Business, 2019.
- [3] VIRTUAL REALITY FOR TRAINING - THE BENEFIT FOR YOUR BUSINESS, TRG Digital, [www.trgdigital.com/blog/employee-onboarding-virtual-reality-for-training/](http://www.trgdigital.com/blog/employee-onboarding-virtual-reality-for-training/).
- [4] "Virtual Reality Market Analysis (US\$ Bn), Insights and Forecast, 2015-2026." *Virtual Reality Market To Exhibit a Remarkable 42.2% CAGR, Moves by Facebook, Google, and Apple to Offer an Advanced User Experience to Boost Growth: Fortune Business Insights K*, Cision PR Newswire, 12 Sept. 2019, [www.prnewswire.com/news-releases/virtual-reality-market-to-exhibit-a-remarkable-42-2-cagr-moves-by-facebook-google-and-apple-to-offer-an-advanced-user-experience-to-boost-growth-fortune-business-insights-300917042.html](http://www.prnewswire.com/news-releases/virtual-reality-market-to-exhibit-a-remarkable-42-2-cagr-moves-by-facebook-google-and-apple-to-offer-an-advanced-user-experience-to-boost-growth-fortune-business-insights-300917042.html).
- [5] Spielberg, Steven, et al. *Ready Player One*. [6] X. Yu, Z. Xie, Y. Yu, J. Lee, A. Vazquez-Guardado, H. Luan, J. Ruban, X. Ning, A. Akhtar, D. Li, *Nature* 2019, 575, 473.
- [7] F. Wen, Z. Sun, T. He, Q. Shi, M. Zhu, Z. Zhang, L. Li, T. Zhang, C. Lee, *Advanced Science*, 2000261.
- [8] C. W. Carpenter, M. G. Malinao, T. A. Rafeedi, D. Rodriguez, S. T. M. Tan, N. B. Root, K. Skelil, J. Ramirez, B. Polat, S. E. Root, *Advanced Materials Technologies* 2020, 1901119.
- [9] C. V. Keef, L. V. Kayser, S. Tronboll, C. W. Carpenter, N. B. Root, M. Finn III, T. F. O'Connor, S. N. Abuhamdieh, D. M. Davies, R. Runser, *Advanced Intelligent Systems* 2020, 2, 2000018.
- [10] C. Dhong, R. Miller, N. B. Root, S. Gupta, L. V. Kayser, C. W. Carpenter, K. J. Loh, V. S. Ramachandran, D. J. Lipomi, *Science advances* 2019, 5, eaaw8845.
- [11] K. Song, S. H. Kim, S. Jin, S. Kim, S. Lee, J.-S. Kim, J.-M. Park, Y. Cha, *Scientific reports* 2019, 9, 1.
- [12] R. K. Adair, *Proceedings of the National Academy of Sciences* 2001, 98, 7253.
- [13] I. Choi, E. Ofek, H. Benko, M. Sinclair, C. Holz, "CLAW: A Multifunctional Handheld Haptic Controller for Grasping, Touching, and Triggering in Virtual Reality", presented at *Proceedings of the 2018 CHI Conference on Human Factors in Computing Systems*, 2018.
- [14] H.-R. Tsai, J. Rekimoto, "ElasticVR: Providing Multi-level Active and Passive Force Feedback in Virtual Reality Using Elasticity", presented at *Extended Abstracts of the 2018 CHI Conference on Human Factors in Computing Systems*, 2018.
- [15] I. Choi, E. W. Hawkes, D. L. Christensen, C. J. Ploch, S. Follmer, "Wolverine: A wearable haptic interface for grasping in virtual reality", presented at *Intelligent Robots and Systems (IROS), 2016 IEEE/RSJ International Conference on*, 2016.
- [16] R. L. Peiris, W. Peng, Z. Chen, L. Chan, K. Minamizawa, "Thermovr: Exploring integrated thermal haptic feedback with head mounted displays", presented at *Proceedings of the 2017 CHI Conference on Human Factors in Computing Systems*, 2017.
- [17] M. Gabardi, D. Chiaradia, D. Leonardi, M. Solazzi, A. Frisoli, "A High Performance Thermal Control for Simulation of Different Materials in a Fingertip Haptic Device", presented at *International Conference on Human Haptic Sensing and Touch Enabled Computer Applications*, 2018.
- [18] Y. Qiu, Z. Lu, Q. Pei, *ACS applied materials & interfaces* 2018, 10, 24807.
- [19] B. Lang, *RoadtoVR*, 2017.
- [20] S. Choi, J. Park, W. Hyun, J. Kim, J. Kim, Y. B. Lee, C. Song, H. J. Hwang, J. H. Kim, T. Hyeon, *ACS nano* 2015, 9, 6626.
- [21] S. Hong, H. Lee, J. Lee, J. Kwon, S. Han, Y. D. Suh, H. Cho, J. Shin, J. Yeo, S. H. Ko, *Advanced materials* 2015, 27, 4744.
- [22] B. W. An, E.-J. Gwak, K. Kim, Y.-C. Kim, J. Jang, J.-Y. Kim, J.-U. Park, *Nano letters* 2015, 16, 471.
- [23] H.-N. Ho, *Temperature* 2018, 5, 36.
- [24] P.-C. Hsu, X. Liu, C. Liu, X. Xie, H. R. Lee, A. J. Welch, T. Zhao, Y. Cui, *Nano letters* 2014, 15, 365.
- [25] S. Ding, J. Jiu, Y. Gao, Y. Tian, T. Araki, T. Sugahara, S. Nagao, M. Nogi, H. Koga, K. Suganuma, *ACS applied materials & interfaces* 2016, 8, 6190.
- [26] J. Jang, B. G. Hyun, S. Ji, E. Cho, B. W. An, W. H. Cheong, J.-U. Park, *NPG Asia Materials* 2017, 9, e432.

- [27] G. Zhang, X. Zhang, H. Huang, J. Wang, Q. Li, L. Q. Chen, Q. Wang, *Advanced Materials* 2016, 28, 4811.
- [28] Y. Lee, M. Kim, Y. Lee, J. Kwon, Y.-L. Park, D. Lee, *IEEE/ASME Transactions on Mechatronics* 2018.
- [29] M. Rull-Bravo, A. Moure, J. Fernandez, M. Martín-González, *Rsc Advances* 2015, 5, 41653.
- [30] M. D. Bartlett, N. Kazem, M. J. Powell-Palm, X. Huang, W. Sun, J. A. Malen, C. Majidi, *Proceedings of the National Academy of Sciences* 2017, 201616377.
- [31] M. Amjadi, Y. J. Yoon, I. Park, *Nanotechnology* 2015, 26, 375501.
- [32] L. A. Jones, H.-N. Ho, *IEEE Transactions on Haptics* 2008, 1, 53.



## 국문 초록

### 가상현실에서 인공 열감 재현을 위한 열-햅틱 전자 피부에 관한 연구

이진우

기계공학부

서울대학교 대학원

가상현실에 관한 기술발전이 이루어지면서 HTC Vive나 Oculus Rift 등 시각 및 청각에 관한 정보를 전달해주는 haptic 장비가 상용화되었다. 하지만, 현재 시각과 청각에 비해서 어떤 사물에 대한 다양한 열적 정보 (thermal information)를 촉각에 대한 haptic 연구는 가상 현실 상에서의 큰 중요성에 비해서 많은 연구가 이루어지지 않았다. 인간의 피부는 압각, 온각, 냉각 및 통각 등 여러가지 정보를 감지할 수 있고 이를 통해서 외부환경과 교류한다. 우리의 일상 생활에서 지속적으로 외부와 열적 상호작용을 하기 때문에 여러가지의 촉각 중에서도 온각과 냉각은 굉장히 핵심적인 역할을 한다. 일례로 시각적이 정보 없이 피부와 사물간의 접촉을 통해서 우리는 상대적인 온도 차이뿐만 아니라 열적 물성(열전도)이 다른 사물들까지 구별할 수 있다. 따라서 인공적으로 정확하게 제어가 가능한 열감을 피부에 구현할 수 있다면 기존의 감각 구현을 더 현실적인 가상현실 시스템을 구축할 수 있게 된다.

본 연구에서는 인체 피부 친화적이고 고 신축성을 갖는 웨어러블(wearable)한 thermo-haptic 소자를 세계 최초로 제작하였다. 펠티어 효과를 이용하여 하나의 소자로 전기 전류 방향을 통해 냉감과 열감을 자유자재로 구현할 수 있게 하였고 PID 제어를 통해서 보다 더 정확한 열적 물성을 표현할 수 있도록 하였다. 뿐만 아니라 본 연구에서의 구리 전극은 구조적으로 늘어날 수 있도록 serpentine 구조로 레이저 가공을 하여 전체 소자가 230%까지 인장이 가능하도록 하여 인체의 굴곡진 표면에 잘 부착할 수 있다. 소자의 성능

을 평가하기 위해서 소자들을 손가락을 움직임을 트래킹할 수 있는 장갑에 부착하여 여러가지 가상현실에서 다양한 인공의 시나리오 (차가운 맥주병을 잡거나 뜨거운 커피잔을 만졌을 때 등) 구현하였다. 또한, 본 소자를 사용하여 온도 구현 뿐만 아니라 열전전도가 다른 물질들의 열적 물성을 표현할 수 있음을 시뮬레이션과 실험적 데이터를 통하여 보여줬다. 이와 같이 피부 친화적이고 웨어러블한 thermo-haptic 소자는 시각과 청각에만 기반한 현재 가상현실 세계에 온각과 냉각을 더하여 보다 더 현실적인 차세대 가상현실 세계를 구축하는데 기여할 수 있을 것이다.

**주요어 :** 전자 피부, 인공 열감, 고 신축성 냉각/가열, 가상 현실

**학 번 :** 2016-30180